

On the nature of the barlens component in barred galaxies: what do boxy/peanut bulges look like when viewed face-on?

E. Athanassoula^{1*}, E. Laurikainen², H. Salo², A. Bosma¹

¹*Aix Marseille Université, CNRS, LAM (Laboratoire d'Astrophysique de Marseille), UMR 7326, 13388 Marseille 13, France*

²*Department of Physics/Astronomy Division, University of Oulu, FIN-90014, Finland*

³*Finnish Centre of Astronomy with ESO (FINCA), University of Turku, Vislntie 20, FI-21500 Pikk, Finland*

Accepted . Received -

ABSTRACT

Barred galaxies have interesting morphological features whose presence and properties set constraints on galactic evolution. Here we examine barlenses, i.e. lens-like components whose extent along the bar major axis is shorter than that of the bar and whose outline is oval or circular. We identify and analyse barlenses in N -body plus SPH simulations, compare them extensively with those from the NIRS0S (Near-IR S0 galaxy survey) and the S⁴G samples (Spitzer Survey of Stellar Structure in Galaxies) and find very good agreement. We observe barlenses in our simulations from different viewing angles. This reveals that *barlenses are the vertically thick part of the bar seen face-on, i.e. a barlens seen edge-on is a boxy/peanut/X bulge*. In morphological studies, and in the absence of kinematics or photometry, a barlens, or part of it, may be mistaken for a classical bulge. Thus the true importance of classical bulges, both in numbers and mass, is smaller than currently assumed, which has implications for galaxy formation studies. Finally, using the shape of the isodensity curves, we propose a rule of thumb for measuring the barlens extent along the bar major axis of moderately inclined galaxies, thus providing an estimate of which part of the bar is thicker.

Key words: galaxies: evolution – galaxies: kinematics and dynamics – galaxies: spiral – galaxies: structure

1 INTRODUCTION

To a zeroth order approximation, disc galaxies can be considered as consisting of two simple components: an axisymmetric disc and a dark matter halo. In the majority of cases, however, it is necessary to consider also at least a classical bulge and/or a bar, two components whose contribution to the total mass and light can be very significant and which can play an important role in the dynamical evolution of the galaxy. A more realistic picture will necessitate yet more components, such as a stellar halo, a thick disc, spiral arms, rings and lenses.

None of these components is simple. To take the bar as an example, its description as an ellipsoid is in most cases oversimplified, because the bar can include ansae (Sandage 1961; Laurikainen *et al.* 2009; Martínez-Valpuesta, Knapen & Buta 2007), can have a rectangular-like outline (Athanassoula *et al.* 1990; Gadotti 2009, 2011) and, when seen edge-on, can have what is referred to as a boxy/peanut/X bulge (hereafter the B/P/X bulge), i.e. an inner part which is vertically thicker than the outer part and has the shape of a box, a peanut, or an ‘X’. The formation and evolution

of this feature have been witnessed in a number of numerical simulations (see Athanassoula 2015 for a review, as well as Combes & Sanders 1981; Combes *et al.* 1990; Pfenniger & Friedli 1991; Raha *et al.* 1991; Berentzen *et al.* 1998; Athanassoula & Misiriotis 2002; Athanassoula 2003; Debattista *et al.* 2004; Athanassoula 2005; Martínez-Valpuesta *et al.* 2006; Berentzen *et al.* 2007; *etc.*).

Simulations of disc galaxies have given us a lot of information on the formation and evolution of bars, the angular momentum exchanged in barred galaxies and the secular evolution that ensues (see Athanassoula 2013, for a review, and references therein). However, in order to safely apply the results of these simulations to barred galaxies and their observations, it is necessary to first make sure that they reproduce well the observed bar properties, be they morphological, photometrical, kinematical or, whenever the simulations allow it, chemical. Morphological comparisons are particularly important, since bar morphological properties have been extensively studied (see Buta 2013a and 2013b for reviews and references therein; see also e.g. Kormendy 1979, Elmegreen & Elmegreen 1985, Erwin & Sparke 2003, Kormendy & Kennicutt 2004, Buta *et al.* 2006 and Laurikainen *et al.* 2009). In contrast, not many simulation studies have focused on morphology. Nevertheless, considerable progress was made by Athanassoula & Misiri-

* E-mail: lia@lam.fr

otis (2002), who reproduced and discussed ansae and who also found that the bar outline in strongly barred simulations was more rectangular-like than elliptical-like, in good agreement with observations (Athanassoula *et al.* 1990; Gadotti 2009, 2011).

In this paper, we will investigate a morphological feature of bars which has only lately been outlined, namely the barlens (often referred to as bl for short). These are lens-like components found in the central parts of barred galaxies and first unambiguously identified, named and discussed by Laurikainen *et al.* (2011) in a study of the NIRSOS survey (Near-IR S0 galaxy Survey), where many images of galaxies with barlenses can be seen (see also Laurikainen & Salo 2015 for an observational review). Viewed face-on, their outline is oval to circular-like, in the direction along the bar major axis they are shorter than the thin bar component (Laurikainen *et al.* 2013) and perpendicular to it they are more extended. They are distinct from nuclear lenses because of their much larger sizes and also from standard lenses (Kormendy 1979; Kormendy & Kennicutt 2004) because they are shorter than bars. Further images of galaxies with barlenses can, in retrospect, be identified in e.g. *The Hubble Atlas of Galaxies* (Sandage 1961), in fig. 2 of Buta *et al.* (2006) and in figs. 8 and 12 of Gadotti (2008). They can also be seen in numerous publications based on the NIRSOS survey (Laurikainen *et al.* 2005, 2006, 2007, 2009, 2010). Here we display in Fig. 1 the NIRSOS image of NGC 4314, a characteristic barlens example (reproduced from Laurikainen *et al.* 2011). In this and many other cases one can see that the bar can be described as a sum of two components, a short, fat, lens-like component, and a thin and much longer component. It is the former of these components that is the barlens. A statistical study of the NIRSOS sample provided useful information on the frequency with which barlenses can be found in disc galaxies and on their sizes (Laurikainen *et al.* 2013). These observational studies, however, were not followed by any theoretical or simulation-based study. We thus ignore whether the barlens is an independent component, or a morphological feature of the bar, and know nothing on how it forms and evolves. We will aim at answering some of these questions in this paper.

For this, we will use a number of high resolution simulations of bar formation and evolution in disc galaxies, and compare the morphology of their bars with that of the bars in the NIRSOS and the S⁴G samples. The NIRSOS sample (Laurikainen *et al.* 2011) consists of about 200 nearby early-type galaxies, mainly S0s, observed in the K_S band using 3–4 m class telescopes in good seeing conditions (full width at half-maximum ~ 1 arcsec). The sample selection criteria include the type ($-3 \leq T \leq 1$), total magnitude ($B_T \leq 12.5$) and inclination ($i \leq 65^\circ$). The S⁴G survey (Sheth *et al.* 2010) is an Exploration Science Legacy Program carried out on the *Spitzer* post-cryogenic mission. It includes more than 2300 galaxies from the nearby Universe ($D < 40$ Mpc) observed with the Infrared Array Camera (IRAC) at 3.6 and 4.5 μ . Its spatial resolution is approximately 2 arcsec.

This paper is organized as follows. In Sect. 2 we summarize theoretical results relevant to bar structure and morphology and in Sect. 3 we present the simulations. In Sect. 4 we compare the morphology and the radial surface density profiles of real to that of simulated galaxies and in Sects. 5 and 6 compare the results of the ellipse fits and decompositions. We discuss our results in Sect. 7 and conclude in Sect. 8. Further observational support for our work is presented in an accompanying observational paper (Laurikainen *et al.* 2014, hereafter L+14).

2 THE STRUCTURE OF BARS

When bars form they are vertically thin, no thicker than the disc they form in. This configuration, however, is vertically not stable (Binney 1978) and, after a relatively short time, the inner part of the bar thickens considerably and protrudes clearly out of the galactic disc (for a review see Athanassoula 2015 and also references therein and in Sect. 1). It is important to stress that it is *not* the whole bar that thickens, but only the inner parts, the outer parts remaining thin (Athanassoula 2005). The bar can thus be considered as consisting of two parts, an outer and an inner part, the former being thin both in the equatorial plane and vertically to it, and the latter being thick in both these directions. Let us now check how theoretical work and observations compare with this picture.

This bar structure can be easily understood with the help of 3D orbital structure (Pfenniger 1984; Skokos, Patsis & Athanassoula 2002a,b). The backbone of the bar is the x_1 family of orbits, which are periodic – closing after one revolution and two radial oscillations – planar and elongated along the bar (Contopoulos & Papayannopoulos 1980; Athanassoula *et al.* 1983). They are stable over most of the family extent, and thus trap regular orbits around them. This family has, nevertheless, a number of vertical instabilities, from which bifurcate other families, often called $x_1 v_1$, $x_1 v_2$, $x_1 v_3$, etc. (Pfenniger 1984; Skokos *et al.* 2002a,b). Their orbits have shapes which, projected on the equatorial plane, are similar to those of the x_1 family orbits, but, contrary to those of the x_1 , they can have a considerable vertical extent. Some of these families have important stable parts, and can thus trap regular orbits around them. These constitute the B/P/X bulge and orbital structure suggests that its major axis length is shorter than that of the bar (Patsis, Skokos & Athanassoula 2002). This has been well confirmed and established by simulations (Athanassoula 2005, and later) by measuring the length of the B/P/X bulge in a side-on¹ view, and the length of the bar in a face-on one and comparing the two lengths. Their ratio, according to orbital structure theory, can take values within a wide range, depending on which perpendicular family sets the extent of the structure. The value of this ratio was considered for the case of M31 by Athanassoula & Beaton (2006) and will be further discussed here for a number of N -body simulations. Let us now briefly review the input from observations.

In our Galaxy the bar is seen edge-on and, due to the location of the sun, is seen only after an integration along lines of sight spanning an angular extent of several degrees. For these reasons it is not possible to have a clear view of the bar morphology, so that the thin and the thick bar components were initially considered as two independent bars, with, moreover, two independent position angles and were thus assumed to rotate at different pattern speeds (Hammersley *et al.* 2000; Benjamin *et al.* 2005; Cabrera-Lavers *et al.* 2007; López-Corredoira *et al.* 2007; Cabrera-Lavers *et al.* 2008; Churchwell *et al.* 2009). More recent work, however, argued clearly that these two bars can simply be the thin and the thick part of a single bar (Athanassoula 2006; Romero-Gómez *et al.* 2011; Martínez-Valpuesta & Gerhard 2011).

Boxy/peanut bulges can of course be easily distinguished in edge-on or near-edge-on external galaxies, since they clearly protrude out of the disc plane. Using photometry, it is also possible to show that there is an associated thin component, embedded in the disc. Lütticke *et al.* (2000) and Bureau *et al.* (2006) used infrared images of samples of 60 and 30 edge-on galaxies, respectively, and

¹ In the side-on view the galaxy is observed edge-on and the line of sight is on the equatorial plane along the minor axis of the bar.

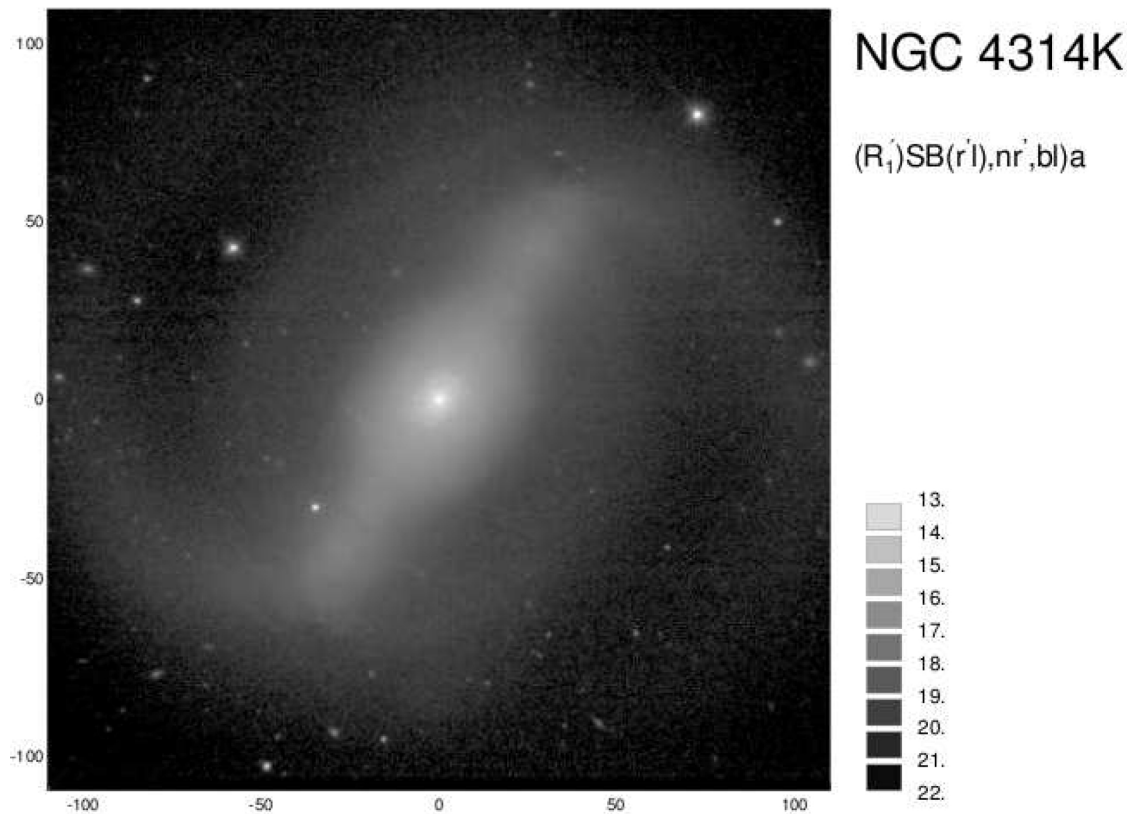


Figure 1. NIRS0S image of NGC 4314. The two components of the bar are clearly discernible. The inner component is shorter and fatter and the outer longer and more elongated (reproduced from Laurikainen *et al.* 2011, by permission of Oxford University press). The units on both axes are arcsec.

analysed the luminosity profile from narrow slits along or parallel to, but offset from, the major axis of each galaxy. They could thus verify the existence of the thin and the thick part of the bar and measure their relative extents, as well as some further relevant quantities. In several cases, however, this task can be rendered very complex by the existence of other thin components in the disc, such as lenses or rings (e.g. Wakamatsu & Hamabe 1984; Kormendy & Kennicutt 2004). Unexpectedly, it is in inclined, but not necessarily edge-on, galaxies that the existence of the two parts of the bar can be seen easiest. This was first noted for NGC 4442 by Bettoni & Galletta (1994), for NGC 7582 by Quillen *et al.* (1997) and for M31 by Athanassoula & Beaton (2006) and Beaton *et al.* (2007), galaxies which have an inclination of 72° , 65° and 77° , respectively. A much larger sample of 78 galaxies, including intermediate inclination angles, was analysed by Erwin & Debattista (2013).

N-body simulations are of course particularly well suited for studying components with such a complex shape as bars, because they can be viewed from any desired angle. Thus, the extent of the thin part of the bar can be measured from the face-on view, while that of the thick part from the side-on one. The snapshot can then be viewed from intermediate inclination angles in order to educate the eye to distinguish the existence and the extent of the thin and thick parts of the bar. This was first performed on simulations by Athanassoula & Beaton (2006), in order to obtain the necessary expertise to distinguish the bar in M31 and get information on its properties, and later by Erwin & Debattista (2013), who extended this work to intermediate inclination angles.

But what about the near-face-on, or moderately inclined galaxies? Answering this question is a primary goal of our paper.

3 SIMULATIONS

For comparisons with observations, we will use two groups of simulations initially made to study the effect of gas and of halo properties on bar formation and evolution. The first one includes simulations with gas and with spherical or triaxial haloes, each one of which will be denoted by 6 characters. The first three are ‘gtr’ (g for gas and tr for triaxial), and are common to all simulations of the group. The last three form a number which distinguishes the various simulations of the group between them. These simulations were described in detail in (Athanassoula, Machado, Rodionov 2013, hereafter AMR13) so we will describe them here only briefly. The second group is designated by the first three letters ‘gcs’ (g for gas and cs for cusp) and has many points in common with the first group (Athanassoula, in prep.). In their initial conditions, all gtr and gcs simulations have a disc and a halo component, the main difference between the two groups being that the halo of the gtr has a small core, while that of the gcs a cusp².

All simulations were run with the GADGET code (Springel, Yoshida, & White 2001; Springel & Hernquist 2002, 2003;

² In radial profiles with a core, the halo density levels off as one reaches the centre, while in cuspy profiles it keeps increasing with decreasing radius.

Springel 2005), a softening of 50 pc for all components, and a cell-opening criterion corresponding to an error tolerance for the force of 0.005^3 . The GADGET code offers the possibility of using several types of particles for the various components of the galaxy. In the following we will use four types, namely: HALO, DISK, GAS and STARS. The DISK particles represent stars already present in the initial conditions and their number remains constant throughout the simulation. But as the simulation evolves, new stars (STARS) form from gas (GAS), so that the number of GAS particles decreases, while that of STARS increases. At any time, the DISK particles and the STAR particles together represent the stars of the galaxy, the DISK component describing older stars than the STARS component. But all the STARS do not represent young stars. Indeed, a fair fraction of them are formed during the first two Gyr and thus have similar age and dynamics to that of DISK particles. The main difference between the two components is that all the DISK particles represent the old stellar population, while a fraction of the STARS describe the young stellar population. This fraction, however, is a strongly decreasing function of time (see Fig. 2 of AMR13), because the simulations do not include accretion.

The DISK has in all cases the same functional form for the initial azimuthally averaged density distribution, namely

$$\rho_d(R, z) = \frac{M_d}{4\pi h^2 z_0} \exp(-R/h) \operatorname{sech}^2\left(\frac{z}{z_0}\right), \quad (1)$$

where R is the cylindrical radius, M_d is the disc mass, h is the disc radial scalelength and z_0 is the disc vertical scale thickness. It also has the same initial radial velocity dispersion profile, namely

$$\sigma_R(R) = 100 \cdot \exp(-R/3h) \text{ km s}^{-1}. \quad (2)$$

For all gtr runs the initial DISK component has a radial scalelength of $h = 3$ kpc, a scale height of $z_0 = 0.6$ kpc, and the mass of each individual particle is $m_{\text{DISK}} = 2.5 \times 10^5 M_\odot$. The corresponding numbers for the gcs simulations are $h = 4$ kpc, $z_0 = 0.6$ kpc, and $m_{\text{DISK}} = 6.25 \times 10^4 M_\odot$.

For the gas, we adopt the same radial profile and the same scalelength as for the stellar disc. This is necessary in order to be able to make sequences of models where only the gas fraction changes, while the rotation curve stays the same for all practical purposes. The gas scaleheight is considerably smaller than that of the stars and its precise value is set by the hydrostatic equilibrium achieved during the iterative calculation of the initial conditions (Rodionov & Athanassoula 2011).

For gtr simulations the haloes have been built so as to have, within the allowed accuracy, in all cases the same spherically averaged initial radial profile, namely

$$\rho_h(r) = \frac{M_h}{2\pi^{3/2}} \frac{\alpha}{r_c} \frac{\exp(-r^2/r_c^2)}{r^2 + \gamma^2}, \quad (3)$$

where r is the radius, M_h is the mass of the halo and γ and r_c are the halo core and cut-off radii, respectively. The parameter α is a normalization constant defined by

$$\alpha = [1 - \sqrt{\pi} \exp(q^2) (1 - \operatorname{erf}(q))]^{-1}, \quad (4)$$

where $q = \gamma/r_c$ (Hernquist 1993). All simulations have $\gamma = 1.5$ kpc, $r_c = 30$ kpc and $M_h = 2.5 \times 10^{11} M_\odot$. The mass of each halo particle is equal to $m_{\text{halo}} = 2.5 \times 10^5 M_\odot$. In this group of

simulations, we consider three different initial halo shapes: spherically symmetric (halo 1), mildly triaxial with initial equatorial and vertical axial ratios 0.8 and 0.6 (halo 2), respectively, and strongly triaxial with initial axial ratios 0.6 and 0.4 (halo 3), respectively. As shown in AMR13, these haloes evolve with time and their shapes become near spherical for halo2 and mildly triaxial for halo 3.

For all gcs simulations, the dark halo density profile follows that of a truncated NFW halo (Navarro, Frenck & White 1996, 1997)

$$\rho_h(r) = \frac{C_h \cdot T(r/r_t)}{(r/r_h)(1 + r/r_h)^2}, \quad (5)$$

where $T(r/r_t) = \exp(-r^2/r_t^2)$, r_h is the halo scalelength, C_h is a parameter defining the mass of the halo, and r_t is a characteristic radius for the tapering. For all gcs models discussed here $r_h = 11$ kpc and $r_t = 50$ kpc. For halo 4 models $C_h = 0.0015$ and for halo 5 ones $C_h = 0.002$. In each of these simulations there are two million particles in the halo.

The initial conditions of both groups were built using the iterative procedure (Rodionov, Athanassoula & Sotnikova 2009; Rodionov & Athanassoula 2011). The corresponding rotation curves of gtr models are given in Fig. 1 of AMR13. The list of the runs analysed here, together with their initial gas fraction and halo type are listed in Tables 1 and 3. To measure the bar strength during the evolution, we use in all cases the maximum of the relative $m=2$ Fourier component, as described in AMR13.

The next step is to use snapshots of the stellar disc component in order to create mock images in form of fits files, which will be analysed in the same way as the observed fits images of galaxies. Due to the relatively small differences between the density distributions of the DISK and STARS, we used these two components together in order to improve the signal-to-noise ratio by increasing the number of particles. Furthermore, as already mentioned above, most of the stars were born in the first few Gyr of the simulation, so that the DISK and STARS together amount to a population compatible with the light emitted by disc galaxies in the near- or mid- IR (Meidt et al. 2012a,b, 2014; Querejeta et al. 2014). The analysis consists mainly of ellipse fits and decompositions, and the techniques and results are described in Sect. 5 and 6.

4 GLOBAL COMPARISONS: MORPHOLOGY AND RADIAL SURFACE DENSITY PROFILES

A simple perusal of the face-on views of the gtr snapshots shown in figs. 4 and 5 in AMR13 shows clearly that, like in observations, simulated bars are not simple ellipsoidal objects, but have a more complex geometry. In the equatorial plane, the inner part of the bar is considerably thicker than the outer thin bar part and has an oval or near-circular shape. A more detailed visual inspection shows that, the morphology of these central components is such that, had they been observed in galaxies, they would have been classified as barlens components. In the rest of this paper we will deepen and substantiate the comparison between barlenses in real galaxies and their counterparts in simulations, and, after establishing that the latter should be called barlenses, we will examine in detail their properties in order to get more information on the barlens structures.

Let us start with comparisons including the morphology and the radial density profiles (Figs. 2, 3 and 4). Fig. 2 compares the results from five simulated galaxies (two left-hand columns) to those of five galaxies from the NIRS0S, or from the S⁴G surveys (two right-hand columns). We carried out this exercise for many more

³ For more information on the algorithmic and numerical aspects of GADGET and the exact definition of its parameters see the manual in <http://www.mpa-garching.mpg.de/~volker/gadget> and the above mentioned references.

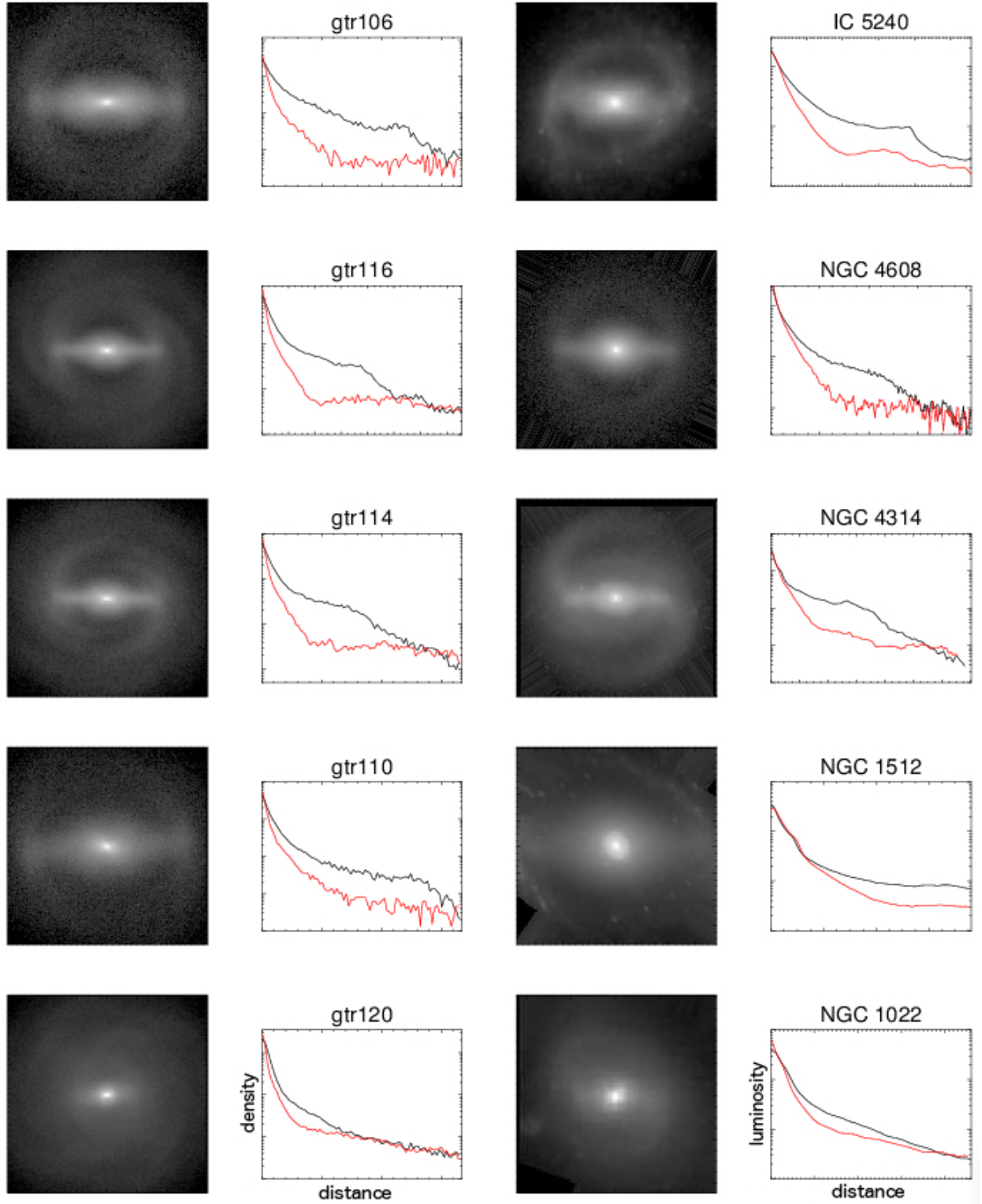


Figure 2. Images and the corresponding surface brightness profiles shown along the bar major (black lines) and minor axis (red lines in the online version). The two left-hand columns show the simulation models and the two right ones galaxies with similar barlenses. The extent of the images has been chosen so as to display in all cases the same region of the galaxy, namely the bar region and, whenever relevant, the inner ring. The galaxy images are either K_s -band images from the NIRS0S Atlas, or $3.6\ \mu\text{m}$ images from the S⁴G survey. Both the simulations and the galaxies are shown in face-on view, and rotated so that the bar appears in a horizontal position. The profiles cover the same regions as the corresponding images. The name of the galaxy, or of the simulation is given above the corresponding radial surface brightness panel. The units of distance, density and luminosity are arbitrary (see text).

snapshots and galaxies, but we will limit ourselves here to five for brevity. It is important to note that the five simulations shown in Figs. 2 were not run specifically so as to model the five chosen galaxies, they were simply picked out by a cursory visual inspection of the images of several snapshots of the gtr and gcs simulations as reasonable matches to the five chosen galaxies. Nevertheless, we get a good resemblance, both for the images and the radial projected density profiles in the region we examine, i.e. a rectangular region of linear extent somewhat larger than the bar region and including, whenever relevant, the inner ring.

The upper row compares simulation gtr106, viewed at a time $t=6$ Gyr after the beginning of the simulation, with an S^4G image of the galaxy IC 5240. This comparison involves two of the longest and most elongated barlenses and quite strong bars. As can be seen in the second panel from the left, the bar projected surface density profiles are quite flat, arguing for a strong bar (see Elmegreen & Elmegreen 1985 and Kim et al. 2015 for the observations and Athanassoula & Misiriotis 2002 for the simulations). Indeed, it was found in AMR13 that gtr106 was one of the strongest bars in that set of simulations (see in particular figs. 4, 5, 7 and 8 in that paper and the corresponding discussions). In this example the extent of the thin bar outside the barlens component is very short, amongst the shortest in our sample. In both the observed and the simulated galaxy profiles this manifests itself by a ledge of very short extent. The part of the profile that is within the ledge rises inwards, but much less steeply than that of classical bulges. This will be discussed further in Sect. 7.3. Note also that in both gtr106 and IC 5240, there is an X-shape in the central regions, even though the simulated galaxy is seen exactly face-on and IC 5240 quite far from edge-on. Such a behaviour is discussed in detail in the accompanying observational paper (L+14).

The second row from the top compares the image of the $t=6$ Gyr snapshot of gtr116 with the NIRS0S image of NGC 4608. In this case, the relevant extent of the thin part of the bar – relative to both the extent of the barlens and the size of the inner ring – is much longer than in the previous example. Note also how thin in the equatorial plane the part of the bar outside the barlens is in the (near-)face-on views of both the galaxy and the simulation snapshot. Further discussion on NGC 4608 is given in Sect. 6.3.1.

The third row compares the $t=6$ Gyr image of gtr114 with the S^4G image of NGC 4314. Both have a fairly round barlens and a strong thin bar component. In the fourth row we compare gtr110 at $t=6$ Gyr with the S^4G image of NGC 1512. Here the barlens is similar to that in the two previous models, but the thin bar is considerably less pronounced, and more dispersed.

Finally, in the bottom row we compare the $t=6$ Gyr image of gtr120 to the S^4G image of NGC 1022. This is the weakest bar in this comparison, and one of the weakest bars in the AMR13 simulations. This can be witnessed also from the radial surface density profiles, which shows clearly that the difference between the profiles along the directions of the bar major and minor axes is less than in the previous cases and that the bar has an exponential profile. The latter according to Athanassoula & Misiriotis (2002) is a sign of a bar weaker than those having a flat profile. In contrast, the barlens is still very prominent.

The right-hand panel of Fig. 3 compares the radial projected surface density profiles along the direction of the major axis of the bar of gtr115 and NGC 5101. Their barlens regions look remarkably similar, although the former was not made specifically so as to model the latter. There is also a further point to note in this figure, which can also be seen in the radial profiles of Fig. 2. The end of the thin bar component can be easily distinguished on these profiles

because of a clear jump, or step, of the radial profile at this radius. On the contrary, the profile has no feature which could indicate the existence of a barlens or its extent. This is presumably because the thin part of the bar extends inwards into the barlens region and thus the profile along the bar major axis includes contributions from both components. It will be discussed further in Sect. 7.

5 ELLIPSE FITTING: TECHNIQUE AND RESULTS

5.1 Techniques

We chose a fitting procedure which is identical to that used for the NIRS0S galaxies, in order to allow comparisons. Given the complex morphological structure of bars, any automatic ellipse fitting would not give useful information concerning the barlens component. For example, isophotes corresponding to the outer regions of the barlens will also trace regions of the outer part of the thin bar component and any automatic ellipse fit would be a compromise between the shape of the barlens and that of the thin outer parts of the bar. Thus, such fits would be strongly biased and useless for our purposes. We therefore resorted to a fully interactive fitting procedure, which, although much more time consuming, guarantees relevant fits.

For the simulated galaxies, before starting the measurements, the simulation units of the image were converted to magnitudes by logarithmic transformation, using a magnitude zero-point of 24 mag/arcsec². The subsequent procedure was followed *identically* for observed and for simulated galaxies. It is very similar to that of masking, where regions which are heavily influenced by other components are masked out. We first inspected all images to determine the magnitude range in which the barlens is best visible, and this was systematically used in all further measurements. We then visualized each individual galaxy separately and chose by eye points on the outermost edge of the barlens which are not affected by the thin part of the bar. Thus these points avoid the region around the direction of the bar major axis. An ellipse was fitted to these points using the same software as for the NIRS0S galaxies. Since the thin part of the bar is thin not only vertically but also on the equatorial plane, the eliminated part is rather restricted and the number of points and the area that is left after elimination are well sufficient to allow an adequate fit, both for observations and for simulations.

Our approach has two important advantages. First, the measurements are not affected by the narrow outer part of the bar (thin bar component), which in automatic ellipse fitting would erroneously make the barlens too elongated. Secondly, it is identical to the one used for the observations, thus best allowing comparisons.

In order to obtain optimum conditions for comparisons of simulations and observations, as well as to minimize the chances of any humanly introduced bias, we proceeded as follows. One of us (EA) chose the snapshots to be analysed in view of the specific goals of our paper, and prepared the fits files. Both the ellipse fits and the decompositions were made by another member of the team (EL), who had also done this same analysis for the NIRS0S sample galaxies. The full description of the runs and of the corresponding snapshots was communicated to the analyser only after she had completed the analysis. As a result, some of the analysis was done two or three times. For example all snapshots in Table 2 were analysed together and we did not simply carry over the results from Table 1 for $t=6$ cases. In this way, some of the snapshots were measured independently two, or three times. A posteriori, we use this to set some estimates of the errors in the ellipse fits. We note that for most cases

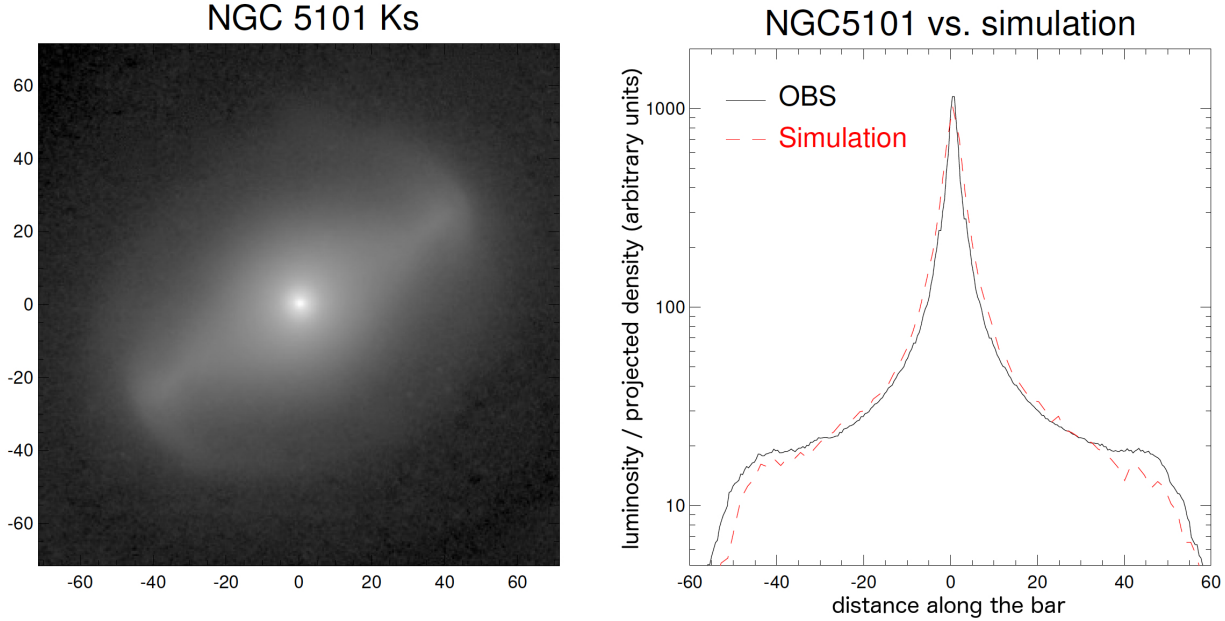


Figure 3. Left-hand panel: the bar region of NGC 5101 in the Ks band (from the NIRS0S sample). Right-hand panel: the surface brightness profiles of the simulation model gtr115 at $t = 6$ Gyr (dashed line, red in the online version) and NGC 5101 (full black line), both shown along the bar major axis. As in the previous figure, only the bar region is shown, so that the sharp edge in the profile is a manifestation of the edge of the bar. The units for the NGC 5101 figure, as well as for the corresponding distance along the bar (black line) are in arcsec, while those of the simulations, are arbitrary. The units for projected density of the simulations as well as for the luminosity for the observations, are arbitrary (see text).

the differences between the two independent estimates of the same snapshots and quantities, are quite small, less or of the order of 10%, showing that the measurements are repetitive, as they should. There is, however, one case, namely gtr101 at $t=6$ Gyr, where the error reaches roughly 20%. This is a very difficult case to measure and, as will be discussed in the next section, we were also unable to make a good decomposition. Furthermore, as will be discussed in Sect. 7, the barlenses in the gas-less simulations are less realistic than those in the remaining runs, with more elongated shapes than usually observed. It is thus not surprising that the parameters of this one case obtained from the ellipse fits are not as robust as those of the other models.

Table 1. Results from our visually driven ellipse fits (see Sect. 5.1) for the barlenses (bl) and the thin part of the bar (bar) in simulation results at time $t=6$ Gyr.

run	Halo profile	initial gas [%]	b/a (bl)	r_{bl}/r_{bar}
gtr101	1: core/spherical	0	0.43	0.77
gtr106	1: core/spherical	20	0.65	0.57
gtr111	1: core/spherical	50	0.95	0.37
gtr116	1: core/spherical	75	0.93	0.45
gtr119	1: core/spherical	100	0.74	0.56
gtr102	2: core/mildly triaxial	0	0.45	-
gtr109	2: core/mildly triaxial	20	0.74	0.47
gtr114	2: core/mildly triaxial	50	0.88	0.46
gtr117	2: core/mildly triaxial	75	0.89	0.81
gtr120	2: core/mildly triaxial	100	0.94	0.51
gtr110	3: core/strongly triaxial	20	0.68	0.49
gtr115	3: core/strongly triaxial	50	0.93	0.52
gtr118	3: core/strongly triaxial	75	0.88	0.53
gtr121	3: core/strongly triaxial	100	0.88	-
gcs006	4: cusp1/spherical	0	0.64	0.94
gcs001	4: cusp1/spherical	20	0.89	0.46
gcs002	4: cusp1/spherical	40	0.96	0.44
gcs003	4: cusp1/spherical	60	0.90	0.52
gcs004	4: cusp1/spherical	80	0.95	-
gcs009	5: cusp2/spherical	60	0.74	0.56
gcs010	5: cusp2/spherical	80	0.91	0.46

Table 2. Results of the axial ratio and relative radial extent of the barlens (bl) component for three simulations, as obtained from our visually driven ellipse fits (see Sect. 5.1).

Time [Gyr] ->	5	6	7	8	9	10
<i>gtr101:</i>						
b/a(bl)	0.59	0.53	0.50	0.47	0.44	0.43
r_{bl}/r_{bar}	0.61	0.78	0.86	0.84	-	-
<i>gtr111:</i>						
b/a(bl)	0.93	0.95	0.53	0.64	0.79	0.83
r_{bl}/r_{bar}	0.39	0.34	0.74	0.69	0.56	0.57
<i>gtr119:</i>						
b/a(bl)	0.72	0.69	0.79	0.79	0.72	0.75
r_{bl}/r_{bar}	-	0.61	0.53	0.61	0.64	0.61

Bar lengths were measured in a similar manner by visually marking the outer edges of the bar. When the simulation model has an inner ring there is some ambiguity, because the bar can be considered to end where the ring starts (i.e. at the inner radius of the ring), or to continue all through the ring, (i.e. to end at the outer radius of the ring), or to end at some intermediate position. Which of these estimates is best is debatable, and may even depend on the case at hand. Here we follow the same definition as in the NIRS0S observations, namely that the end of the bar is defined by the ridge-line of the ring, in order to allow comparisons between simulations and observations, particularly since the bar length estimate will be used further in the decompositions (see Sect. 6).

5.2 Results

Table 1 gives information on the ellipses fitted to the face-on images of the simulation snapshots at time $t = 6$ Gyr from the beginning of the run. The first three columns give the simulation name, its initial halo characteristics and the initial fraction of its baryons that is in the form of gas, respectively. The fourth and fifth columns give the axial ratio of the barlens component and its extent along the bar major axis normalized by the bar length. The five packages in this Table (separated by a blank horizontal line) correspond to the five different halo radial profiles, halo 1 to halo 5, described in Sect. 3. Results from different viewing angles will be discussed later (see Table 5 and Sect. 6.3.3).

In this, as in all subsequent tables, a dash as an entry means that no safe estimate for this quantity could be found. This occurs particularly, but not exclusively, in cases like gcs004 or gtr121, where the thin part of the bar is so weak that it is very hard to measure its extent as reliably as we did for other simulations. We will therefore omit these cases from most of the following discussions, where the barlength estimate is necessary. Some values for gtr101 and gcs006 are also unsafe because the barlens covers most of the thin bar extent and the barlens shapes are less realistic (Sect. 7). We have, nevertheless, kept some of these value in the tables as a reminder that there are cases where the barlens extent covers a very large fraction of that of the bar.

The two most elongated barlenses are those of gtr101 (axial ratio 0.43) and gtr102 (0.45), both cases being simulations with no gas and amongst the strongest bars in AMR13. The remaining simulation with no gas (gcs006) has an axial ratio of 0.64. Note

that these simulations are the ones for which the ratio of barlens to bar extent is the most unsafe. In all simulations with gas, the barlenses are considerably nearer to near-circular, with most axial ratios between 0.7 and 1.0. The ratio of the extent of the barlens to that of the thin bar component has a lower limit of ~ 0.4 and an upper one of ~ 0.9 . We will discuss the implications of this result in Sect. 7.6.

Table 2 gives information on the barlens shape and on the ratio of its extent to that of the bar, for three simulations and six snapshot times, spaced by 1 Gyr. These three simulations are good examples of a very strong, an intermediate and a weak bar. This table shows clearly that the fractional change of the barlens shape, as well as of its extent relative to the bar vary considerably from one case to another. Amongst the three, the least variation is found for gtr119, where the changes are barely of the order of 10 per cent, and the most for gtr101 where the changes are nearly of the order of 50 per cent. In general we can see that the runs that showed the most secular evolution (see AMR13) show also the largest changes of the barlens axial ratio and of its extent relative to that of the bar, as expected.

Simulation gtr111 has two distinct time intervals in its evolution with different properties for the barlens in each. For times up to and including 6 Gyr the barlens is near-circular and relatively short, with axial ratios larger than 0.9 and a length relative to the bar length of less than 0.4. It then shows a clear change between 6 and 8 Gyr, while from 8 Gyr onward it is considerably thinner and longer, with average axial ratio and average relative extent of 0.75 and 0.6, respectively. It is interesting to note that in the range between 6 and 8 Gyr the increase of the bar strength with time shows a change of slope, turning from a rather fast to a more moderate growth (fig. 7 of AMR13 or fig. 1 of Iannuzzi & Athanassoula 2015). In this same time range, the increase of the peanut strength also changes from rather fast to more moderate (fig. 2 of Iannuzzi & Athanassoula 2015). This constitutes a further argument for a strong link between the barlens and the bar. Note that no buckling episode (i.e. no asymmetry) can be seen by eye during this time range, or at any other time. A more in depth analysis of this interesting behaviour is beyond the scope of this paper.

6 DECOMPOSITIONS: TECHNIQUE AND RESULTS

6.1 The components

The simulation models discussed in the previous section were decomposed into multiple structural components, fitting the bar with two separate functions. We used GALFIT (Peng et al. 2010) with the auxiliary illustration programs described in Salo *et al.* (2015), and the same approach as that used for the observed images in the NIRS0S Atlas (Laurikainen *et al.* 2010). For the weighting of the simulation images a constant sigma-image was used because this mimics well the typical uncertainty map for ground based near-IR images, where the noise is dominated by the sky background. All fitting functions have generalized elliptical isophotes (Athanassoula *et al.* 1990), so that:

$$(|x|/a)^c + (|y|/b)^c = 1, \quad (6)$$

where c is a shape parameter and a and b are the major and minor axes, respectively. We will denote their axial ratio by $q = b/a$. An isophote is boxy when its shape parameter $c > 2$, diamond-like when $c < 2$, and elliptical when $c = 2$ (see fig. 1 of Athanassoula

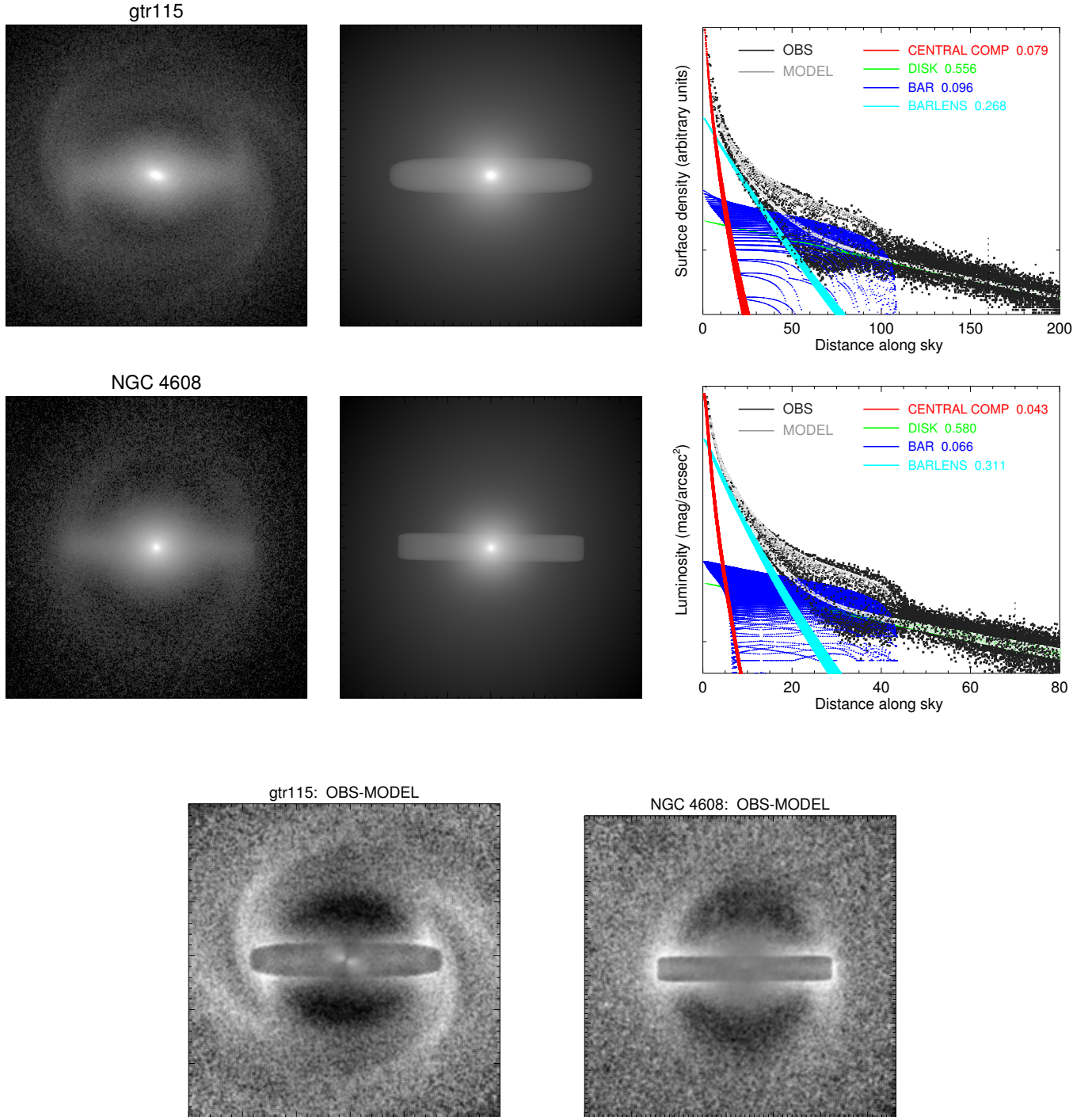


Figure 4. Images and their decompositions for the simulation model gtr115 (upper panels), and the galaxy NGC 4608 observed in K_s -band (middle panels). The left-hand panels in the two upper rows show the images and the middle ones show the sum of the components obtained from their decomposition. All the images are shown in face-on view and cut so as to show only the bar and inner ring region. The right-hand panels in the two upper rows show two dimensional representations of the surface brightness profiles of the images (black dots), as well as of the GALFIT decomposition models fitted for the different structure components (red dots for the central peak component, green for the disc, dark blue for the bar and cyan for the barlens). The total decomposition models are shown with light grey dots. ‘Bar’ in the profiles refers to the thin, elongated bar component and ‘barlens’ to the thick component, which is not far from circular. The abscissa in the right, second-row panel is given in arcseconds. In the upper right panel the abscissa is scaled so that the bar length is roughly the same for the galaxy and for the simulation. The vertical black dotted lines in the profile figures (roughly at a distance from the centre of 160 and 70 pixels for the upper and middle panels, respectively) show the edges of the images in the left and middle panels. The two figures in the bottom panel show the residuals for the simulation (left-hand panel) and for the galaxy (right-hand panel). In the dark areas the decomposition model has higher values than the simulation/galaxy, the opposite being true for the white ones. Note that no spirals or ring components were used in the decompositions, which accounts for the white or very light grey areas in the two lower panels. The method and the functions used for making the decompositions are described in the text.

et al. 1990). For the radial projected surface density of the disc component we used an exponential function:

$$\Sigma(r) = \Sigma_{0,d} \exp[-(r/h_d)], \quad (7)$$

where $\Sigma_{0,d}$ is the disc central surface density, and h_d is the disc radial scalelength. The thin bar component is described for $r \leq r_{out}$ by a modified Ferrers function:

$$\Sigma(r) = \Sigma_{0,th} [1 - (r/r_{out})^{2-\beta}]^\alpha, \quad (8)$$

where $\Sigma_{0,th}$ is the central surface density of the thin bar component, r_{out} is its distance from the centre to its outer edge, β gives its central slope, and α is a measure of the sharpness of its outer truncation (Ferrers 1877). For $r > r_{out}$ the projected surface density is set equal to zero.

There is no preferred function for the bar component. One possibility is the Sérsic function:

$$\Sigma(r) = \Sigma_{0,bl} \exp[-(r/h_{bl})^{1/n}], \quad (9)$$

where $\Sigma_{0,bl}$ and h_{bl} are the bar central surface density and its scale parameter, respectively, and n the Sérsic index. This does not have a cut-off at some outer radius. An alternative is to use a modified Ferrers function (equation 8) which does have a cut-off, but is otherwise less well suited. We tried both and adopted the one which gave a better fit for each case.

We also include in our decompositions an extra Sérsic profile to fit the centre-most regions where there is typically a central peak (spike) in the surface brightness profile, which we need to account for in order to obtain a good fit to the bar. Such a component is also found in observed galaxies and is accounted for in the same way, i.e. with a supplementary narrow Sérsic profile. Simulations necessarily have a softening which smooths out the central component. However, the simulations we consider here are of high resolution, with a softening of 50 pc. Similarly, the NIRS0S observations have a full width half-maximum of the PSF of 1 arcsec, while for the S⁴G observations this is roughly 2 arcsec. For NGC 4314, shown in Fig. 1, this gives 47 and 94 pc, for the two samples respectively. We thus see that the simulations and the NIRS0S have very comparable high resolutions, while the S⁴G sample has a somewhat lower resolution. The above estimates argue that, for both simulations and observations, this spike is real but, at the risk of erring on the side of caution, we will not discuss its parameters further here and, unless otherwise mentioned, none of the flux values (be they that of the bar, thin bar, or that of the total flux used for normalization) include the contribution of the spike.

There are two important points to note in the above choices of the components and of their properties. The first one is that we adopted generalized ellipses, which is particularly crucial for the thin bar and bar component, because their isophotes do not have an elliptical shape. The second important point is that we describe the bar as a sum of two components. This is necessary because, as was initially discussed by Athanassoula (2005), the shape of the bar is very complex, composed of two parts with very different properties: an outer thin, and an inner thick component, with different radial profiles. Such a component does not exist in the GALFIT program, so we have to resort to using two independent components to fit the bar adequately. Both components are crucial for the type of work we need to do. Note that a second component for the bar has been introduced in some barred galaxy decompositions already about 10 years ago (Laurikainen *et al.* 2005). To our knowledge, however, it has not as yet been used for any decompositions of simulation results.

Table 3. Flux ratios of the bar component as obtained from the decompositions of snapshot images at $t = 6$ Gyr.

Run	Halo	initial gas [%]	F_{bl}/F_{thin}	F_{bl}/F_{tot}
gtr106	1: core/spherical	20	2.6	0.33
gtr111	1: core/spherical	50	0.93	0.13
gtr116	1: core/spherical	75	1.2	0.15
gtr119	1: core/spherical	100	5.8	0.13
gtr109	2: core/mildly triaxial	20	3.1	0.39
gtr114	2: core/mildly triaxial	50	3.5	0.25
gtr117	2: core/mildly triaxial	75	0.4	0.26
gtr120	2: core/mildly triaxial	100	9.5	0.19
gtr110	3: core/strongly triaxial	20	6.7	0.44
gtr115	3: core/strongly triaxial	50	1.9	0.19
gtr118	3: core/strongly triaxial	75	3.9	0.14
gtr121	3: core/strongly triaxial	100	-	0.18
gcs001	4: cusp1/spherical	20	-	0.21
gcs002	4: cusp1/spherical	40	2.9	0.18
gcs003	4: cusp1/spherical	60	3.5	0.20
gcs009	5: cusp2/spherical	60	2.3	0.18
gcs010	5: cusp2/spherical	80	4.4	0.21

6.2 The fitting procedure

In our GALFIT decompositions we used the same procedure as in observational studies (Laurikainen *et al.* 2010). The bar length was set to be the visually estimated outer edge of the bar obtained during the ellipse fitting work (Sect. 5). This was reasonable, because otherwise GALFIT would try to include the inner ring as part of the bar. Furthermore, we fixed the bar size and axial ratio to the values found from the ellipse fits. After that, we started the fitting process, iterating in order to find the appropriate values for the remaining parameters, and making a large number of trials until a ‘final’ decomposition was adopted. The choice was based on inspecting the profile fitting, and on a comparison of the decomposition model with the original image. Generally, it was not possible to get good fits by setting free all parameters at once. We thus fixed some values and let GALFIT search for the remaining. Once a reasonable value was found for one parameter, it was fixed and others set free. These cycles were continued until the final decomposition was reached. The number of necessary trials varied from one image to another, but was always large. Also the sequence in which we set the parameters free varied from one case to another, although we often found easiest to obtain first reasonable values for the orientations, the fluxes and the disc scalelength.

6.3 Results

6.3.1 Comparing decomposition results of an observed and a simulated galaxy

Fig. 4 compares the decomposition results for NGC 4608 from the NIRS0S sample and for simulation gtr115. The left-hand panels show the respective images and the middle ones the superposition of the components resulting from the decompositions. This comparison is made more quantitative in the right-panels panels, which show the radial surface density profiles of the various components separately, as well as the totals. Such plots are standard in observa-

Table 4. Time evolution of the relative flux of the barlens component, as obtained from decompositions of the simulation images.

Age -> (Gyr)	4	5	6	7	8	9	10
<i>gtr111:</i>							
F_{bl}/F_{thin}	0.44	0.81	0.95	-	2.35	1.39	1.36
F_{bl}/F_{tot}	0.03	0.08	0.13	-	0.22	0.20	0.21
<i>gtr119:</i>							
F_{bl}/F_{thin}	6.16	6.28	5.81	2.87	2.53	1.79	1.79
F_{bl}/F_{tot}	0.11	0.16	0.16	0.16	0.17	0.20	0.20

tional studies and are made so as to include information from non-axisymmetric 2D decompositions in radial profiles. Every black point is a pixel from the image and every red (green, dark blue and cyan) point is a pixel from the central peak component (disc, bar and barlens component, respectively). Thus this plot can be seen as a sequence of radial surface density profiles for each component separately, the total model and the image. From all these plots we can see that the simulation snapshot describes NGC 4608 quite successfully, even though it was not made specifically for that purpose but is just a closely resembling snapshot from the AMR13 sample.

The lower panels of Fig. 4 present the residual maps, which can attest to the quality of the decomposition in the relevant area. In our decomposition the disc model is axisymmetric, so the minima on the direction of the bar minor axis above and below the bar, seen both in the observed and the simulated galaxy, can not be accounted for. This leads to the dark areas in these regions. Furthermore, no spiral or ring component was included in the decomposition, since this is not the object of our study. This explains the residuals outside the bar region where such components are present in the simulation and galaxy. Note also that the spirals in the outer parts of the simulation are not present in the galaxy image. This can be understood because the simulation has at the time of the comparison still nearly 6% of its baryons in the form of gas, which NGC 4608, being a SB0 without HI detection, does not have. Thus we can conclude that the decomposition is satisfactory in the bar region under study, but further components need to be introduced in order to get a better model for the whole galaxy.

6.3.2 Decomposition results for a number of simulations and times

In Tables 3 and 4 we give the decomposition results for the flux ratios of all our models. The former has the same layout as Table 1, except that in the fourth column we give the values of the barlens fluxes, F_{bl} , normalized to the flux of the thin bar component, F_{thin} , and in the fifth one the same quantity, now normalized to the total flux of the galaxy, F_{tot} . Table 4 has a layout similar to that of Table 2, but gives information on the barlens flux normalized by the flux of the thin bar component (upper line for each simulation), and by the total flux (lower line).

For simulations with no gas initially, e.g. gtr101, gtr102, gtr003 and gcs006, it is unclear whether a two bar component fit is necessary and decompositions with a single bar component can not be excluded. We therefore do not include these simulations in Tables 3 and 4. There are also decomposition difficulties for snap-

Table 5. The effect of the viewing angle on the properties of barlenses for the simulation model gtr111 at time $t=6$ Gyr

Bar position angle	inclination	b/a	F_{bl}/F_{thin}	F_{bl}/F_{tot}
00	00	0.96	0.95	0.130
00	30	0.77	0.95	0.110
30	30	0.80	0.99	0.116
60	30	0.75	1.30	0.135
00	60	0.64	0.50	0.054
30	60	0.78	0.79	0.089
60	60	0.66	0.31	0.058
90	60	0.86	1.07	0.118

shots at the other extreme of the gas fraction, e.g. for gtr121, where the thin bar component is too weak and short to allow a reliable decomposition. Simulation gtr117 was also difficult to decompose and the values given are not as reliable as those of other simulations. The cases which are difficult to decompose presented also difficulties in the ellipse fits. We will therefore single them out, or omit them from many of the following discussions, since the results, if at all available, are less reliable than those of the remaining runs.

In cases where the thin bar component is very short and difficult to discern, the F_{bl}/F_{thin} takes very large values, but these are very unsafe because of the large uncertainties for F_{thin} . They should thus be used only with caution. This is presumably the case e.g. for the three earlier times of gtr119 in Table 4. For such cases, but also more generally, the F_{bl}/F_{tot} values are much safer to use.

6.3.3 Decomposition tests

We have so far considered only face-on views with the bar major axis along the x axis. Here we will present decomposition results for different viewing angles. For this we used simulation gtr111 at $t=6$ Gyr, whose barlens is near-circular, with an axial ratio of 0.96. We viewed the snapshot after a rotation in the disc plane, to put the bar major axis at a different angles with respect to the galaxy major axis. We then inclined it by another angle. The results are given in Table 5. The first two columns give the viewing angles, the third one gives the axial ratio of the barlens component as obtained from the ellipse fits and the last two give the relative barlens fluxes. The results for the face-on view are given in the first row, and examples with 30° inclination in the next three rows. The errors are of the order of 10–20 per cent, i.e. sufficiently small to allow considerable analysis and statistics. If, however, we consider inclinations as high as 60° (four last lines of Table 5), the errors are higher. This argues that for some statistical work involving barlenses it may be necessary to introduce a lower inclination cut-off than the commonly used 60° or 65° . How much the results are affected by a given inclination should vary from one case to another and should in particular depend on the extent of the barlens above and below the equatorial plane.

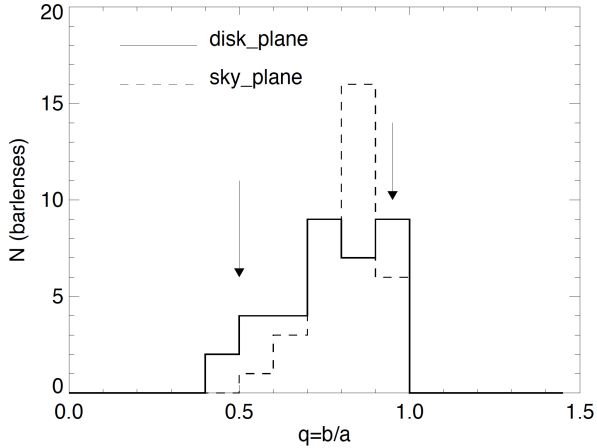


Figure 5. Number histogram of the minor-to-major axis ratios of barlenses in the NIRSOS Atlas. The full black line shows the measurements in the disc plain, and the dashed line the same galaxies in the sky-plane. The arrows mark the minimum and maximum of this parameter for our simulation models (in the plane of the disc).

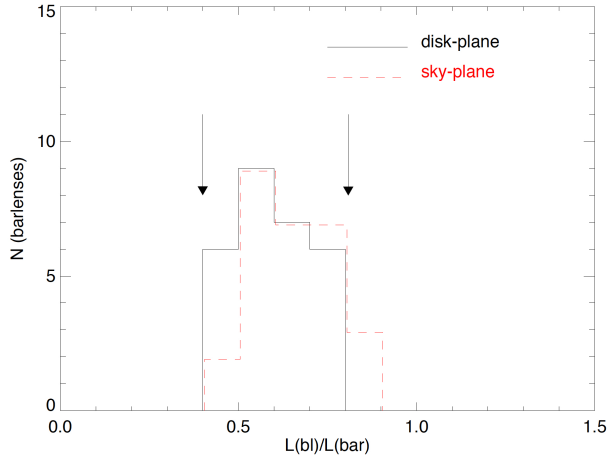


Figure 6. Number histogram of the sizes of barlenses for the galaxies in the NIRSOS Atlas, normalized to the corresponding bar length. The black full line shows the measurements in the disc plain, and the (red online) dashed line the same galaxies in the sky-plane. The arrows indicate the minimum and maximum of the same parameter in our simulation models (in the disc plane). The sizes of structures are measured in a similar manner for the simulation models and for the observed galaxies.

7 DISCUSSION

7.1 Range of values for the barlens relative lengths and axial ratios

Let us now compare the range of values for the axial ratios of the barlens components in observations and in simulations. The former can be found for all galaxies with a barlens component in Table 5 of Laurikainen *et al.* (2011) and their histogram is plotted here in Fig. 5, both in the sky-plane and in the galactic disc plane (assuming thin structures). The ellipticities for the simulations have been obtained from the ellipse fits described in Sect. 5. These sim-

ulations, however, were made in order to understand the effect of gas and of the dark matter halo on bar formation and evolution (Sect. 3) and do not necessarily cover the parameter space in the same way as the barred galaxies in NIRSOS. Furthermore the de-projection of observed galaxies, particularly barred, always entails some uncertainty. It is thus more meaningful to compare the range of allowed values than the distribution of values given by the whole histogram. We find that the range of ellipticities obtained for barlenses in our simulation models (marked with arrows) fits well the range defined by the observations. Furthermore, barlens ellipticities of the gtr models with initial gas fractions of 0.5, 0.75 or 1.00, are within the range of 0.7–1.0, where most of the observed ellipticities are found.

The distribution of barlens sizes, normalized to the bar length, as obtained from the NIRSOS sample, are shown in Fig. 6, again given separately for the disc and the sky planes. In the comparison with simulations we omitted gcs006, because its measurements are much less reliable than those of the other simulations (see Sect. 5 and 6). Fig. 6 shows clearly the comparison of the range of values obtained from simulations to the range of observed ones is most satisfactory.

7.2 Comparing the face-on and the side-on views

Simulations have an important advantage over observations in that they allow the viewing of an object from any desired viewing angle. We will use this here in order to study the 3D structure of the barlens component. In the left-hand and middle panels of Fig. 7 we show two snapshots viewed from three different angles. The snapshots correspond to the disc component of simulations gtr116 and gcs001, both at $t=6$ Gyr. In the lower sub-panels they are viewed face-on and in the upper ones edge-on. The central sub-panels correspond to an intermediate viewing angle of 45° . In both cases the bar is oriented along the x axis, to facilitate comparisons. These two snapshots were chosen because they are good examples of specific morphological features which we wish to discuss here.

The face-on and intermediate views in Fig. 7 show that the edge of the barlens component at and around the direction of the bar minor axis is relatively sharply defined, as witnessed by the crowding of the isodensities in that region, arguing for a correspondingly sharp decrease of the barlens density profile. This is in good agreement with the strong decrease of the surface density in the barlens region seen on the minor axis profiles in Fig. 2. In contrast, the only crowding of isodensities in the direction of the bar major axis is at the end of the bar. No corresponding feature is seen at the end of the barlens, in good agreement with Fig. 3 and the corresponding discussion at the end of Sect. 4.

A further interesting point to note is the difference that the inclination makes to the shapes of both the thin bar component and the barlens. This can be clearly seen by comparing the shape of the isodensities in the face-on and the intermediate view. In the face-on view, the thickness of the bar along the direction of its minor axis has a maximum at $x=0$, then decreases with increasing distance from the centre to reach a minimum before increasing again in the region of the ansae. For example for gcs001 at $t=6$ Gyr (left-hand panel of Fig. 7), the minimum thickness of the projected surface density isocontours occurs somewhere around 4 kpc from the centre (measured along the bar major axis). Then the bar outline starts becoming thicker again. Such a minimum is not visible in the intermediate view (inclination angle of 45°), where the barlens isophotes near the bar minor axis are flat, presumably due to the projected contribution of the B/P bulge which extends more than a

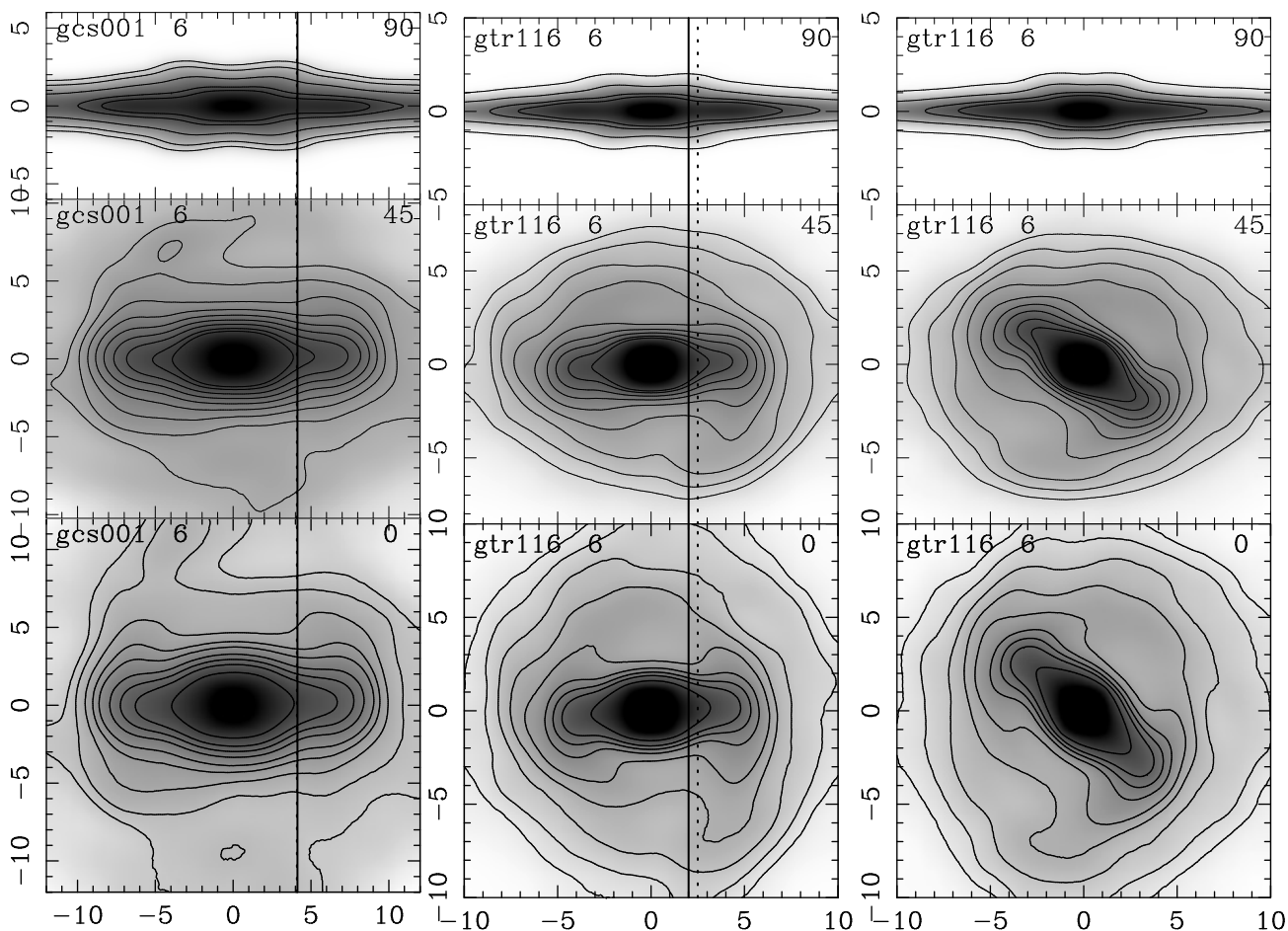


Figure 7. The left-hand and middle columns show grey-scale plots and isodensities of three views of simulation gcs001 (left) and gtr116 (middle), both at $t=6$ Gyr. In the lowest sub-panels the simulations are viewed face-on, in the top ones side-on and in the central ones at 45° . The grey-scale levels are logarithmically spaced and the isodensities are at levels chosen to show best given morphological features discussed in the text. The vertical solid lines extending through all three sub-panels show the extent of the barlens component in all three views, as measured by the ellipse fits (Sect. 5). The vertical dashed lines show the extent of the B/P/X bulge. The right-hand column illustrates again gtr116, but now with the bar at 45° from the line of nodes. In the upper left corner of each sub-panel we give the simulation name and snapshot time in Gyr and in the upper right one the viewing inclination angle in degrees.

kpc above the equatorial plane. Similar results can be seen in the middle panel for gtr116 at $t=6$ Gyr.

The solid vertical lines extending through all three sub-panels show the extent of the barlens along the bar major axis, as measured from the ellipse fits (Sect. 5). There are also vertical dotted lines, which show the horizontal extent of the B/P bulge as estimated from the side-on view. Comparing their locations to that of the solid lines it is clear that the end of the barlens coincides, to within the estimation accuracy, with the end of the B/P bulge. In fact in some cases, as e.g. gcs001 at $t=6$ Gyr (left-hand panel of Fig. 7), the two estimates coincide to within the thickness of the lines in the plot, so that no dotted line can be seen. We repeated this exercise for a number of snapshots (simulations and times) and always found the same qualitative result. For the ratios of the extent of the barlens to that of the B/P bulge we found a median of 0.96, a mean of 0.97 and an absolute deviation of 0.14, which argues that the barlens and the B/P extent are equal to within the measuring errors. This strongly argues that the barlens and the boxy/peanut bulge are one and the same component, and not two separate components, or two separate parts of the bar. They are simply viewed from a different viewing angle, near face-on for the barlens and near edge-on for the B/P/X bulge. One would then expect that the fraction of observed

galaxies having either a barlens or a B/P/X should be independent of the viewing angle, and this is indeed what we found and reported in the accompanying observational paper (L+14).

We thus confirm that, as argued by Athanassoula (2005), bars are composed of two parts, an outer one being both vertically and horizontally thin, so that it can be called the thin bar component, and an inner one which is vertically thick and also fatter in the equatorial plane. This can be called the thick part of the bar, or the B/P/X bulge, or the barlens; all three names describing the same part of the bar.

Our plots allowed us to obtain a rule of thumb that can give us information on the extent of the B/P/X/barlens component when the galaxy is viewed near-face-on. Indeed, as already mentioned, the shape of the isophotes in the barlens region is very different from that in the thin bar part. This makes the isophotes change curvature, from orienting their concave part towards the bar major axis to being rather flat, or orienting their convex part towards the bar major axis. The point or region where this change of curvature occurs gives a good estimate of the length of the barlens component. When applying this rule of thumb, it is also recommended to use several isodensity contours, since some show this minimum or flattening clearer than others.

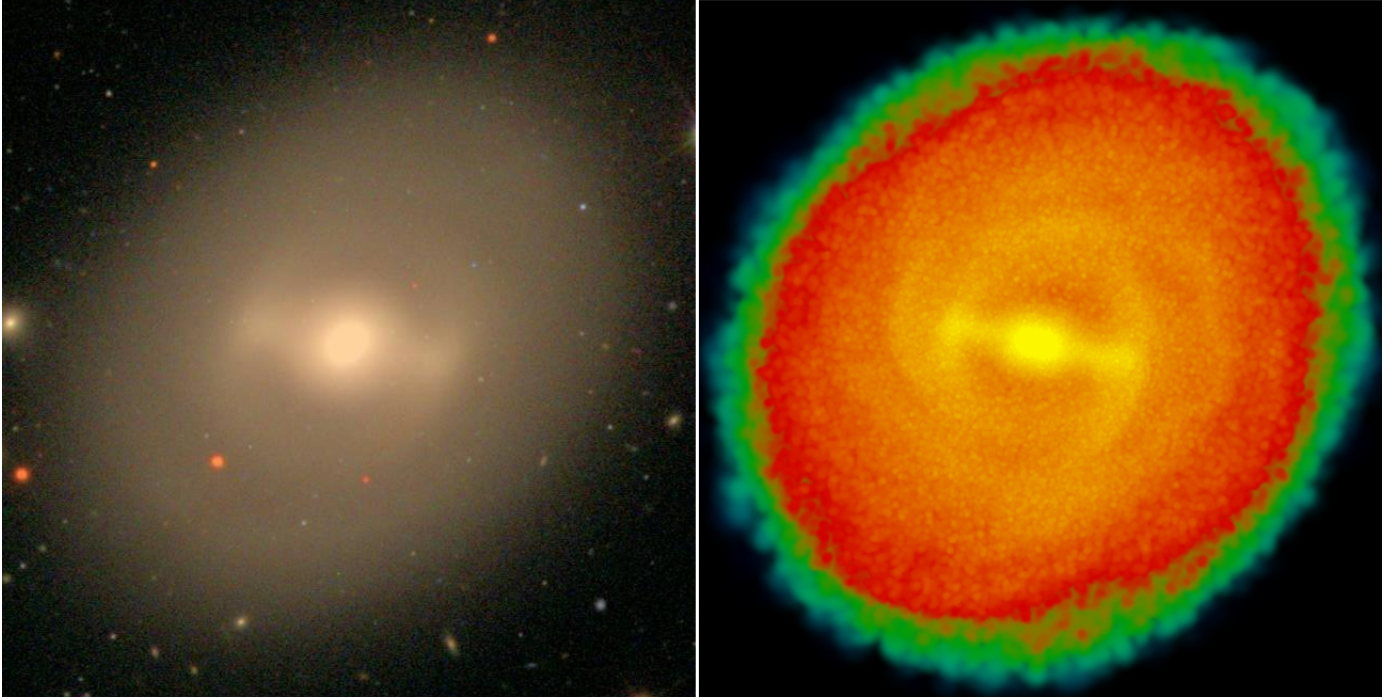


Figure 8. Comparison of a simulation snapshot (right-hand panel) with an SDSS image of NGC 936 (Hogg, Blanton and the SDSS collaboration, as in the Near Extragalactic Database). Note the resemblance between the two morphologies in the bar region. The simulation has, by construction, no classical bulge component, the inner component being a barlens when viewed face-on and a B/P/X bulge when seen edge-on. We discuss the implication of this comparison in Sect. 7.3.

This rule of thumb works well near the face-on geometry, but it needs to be extended to be applicable to inclination angles up to say 45° . Fig. 7 shows that for such inclinations and when the bar is near the line of nodes, the isodensities near the bar minor axis are not curved as for the face-on view, but flat (straight). Thus the bar isodensities have two flat sections, both roughly parallel to the bar major axis. The location where any one of these two sections joins the part of the isodensity that orients its concave part towards the bar major axis is the end of the barlens. As before, it is more reliable to use a number of isophotes. It is not necessary to extend this rule of thumb to yet higher inclinations (i.e. nearer to edge-on) because there the vertical extent of the barlens makes it anyway easier to find its radial extent (Athanassoula & Beaton 2006; Erwin & Debattista 2013).

We checked our rule of thumb by applying it to a number of snapshots seen from different viewing angles, and found that it fares very well for most morphologies, particularly after one's eye has gained some expertise in detecting the correct features. There may, nevertheless, be some bar morphologies to which it can not be applied, such as relatively fat bars with near-elliptical isodensities. Our rule of thumb is of course rather crude, but certainly safer than using a constant value for the ratio of the bar and barlens extents, as has been previously proposed, because as we saw in Sect. 7.1 and will further discuss in Sect. 7.6 the ratio of these two extents covers a wide range of values both in the observations and in the simulations.

7.3 Can some barlenses be partly or fully mistaken for classical bulges?

In Fig. 8 we view a further comparison between simulations and observations. The left-hand panel shows an image of the barred

galaxy NGC 936, obtained by combining the g, r and i images from the SDSS. The right-hand panel displays gtr116 at time $t = 6$ Gyr, viewed from angles such that it mimics best NGC 936. This simulation was not specifically run so as to model NGC 936, yet the bar regions in the observations and in the simulations have a very similar morphology. The most important thing to note, however, is that this simple visual inspection of the central region of both NGC 936 and the simulation could lead to the conclusion that both have a classical bulge, while at least for the simulation we are sure, by construction, that it has no such component. This shows that a barlens component may be mistaken for a classical bulge, if morphology is the only available information.

Could photometry reveal whether the inner component is a barlens or a classical bulge? Fig. 3 shows that, both in observations and in simulations, barlenses can produce a clear central peak in the radial luminosity profile. This, however, is less sharp than that of a classical bulge, and quantitative measurements of the Sérsic index should be able to distinguish between the two, since the standard value for a classical bulge is larger than 2 or 2.5 (Kormendy & Kennicutt 2004; Drory & Fisher 2007; Fisher & Drory 2008), while that of the barlens is considerably smaller ($L+14$). Thus, the answer to our initial question is that accurate photometry should most probably be able to distinguish between a classical bulge and a barlens component.

Could colours, or population synthesis help us distinguish between these two types of components? Indeed, B/P/X bulges are formed from the vertical instabilities of the bar, i.e. such bulges are constituted of stars initially in the disc. In contrast, the most standard formation mechanism of classical bulges is from mergings occurring early on in the galaxy formation process, before the formation of the thin disc. Thus if the inner component is composed of stars that are older and redder than the disc or bar, then

it would be a classical bulge and not a barlens. This colour difference, however, is not a necessary condition, since classical bulges can also form from later occurring minor mergers or they may have later gas accretion (e.g. Aguerri, Balcells & Peletier 2001; Coelho & Gadotti 2011), in which cases their stellar populations could be younger and bluer than the disc, or they could include a younger sub-population. Thus, in some cases it may be possible to distinguish classical bulges from barlenses by their colours or with the help of population synthesis, but in others not.

Orbits in barlenses are very different from those in classical bulges, so detailed kinematic observations could be very helpful in distinguishing between the two types of components. Specifically for NGC 936, signatures of kinematics which are not compatible with pure classical bulges have been discussed by Kormendy (1983, 1984); Kent & Glaudel (1989) and Cappellari (2013, private communication, see www.eso.org/sci/meetings/2013/MORPH/Videos/Day-4/morph2013Athanasoula.mp4; see also Cappellari *et al.* 2011 and Cappellari *et al.* 2013). Unfortunately though, such detailed kinematics are available only for relatively few galaxies⁴.

All the above argue that, for galaxies which are seen near to face-on and for which neither detailed kinematics nor photometry are available, barlenses could be mistaken for classical bulges. The picture is yet more complex because B/P/X/bl components and classical bulges can well coexist in galaxies (e.g. Athanasoula 2005; Kormendy & Barentine 2010; Nowak *et al.* 2010; Mendez-Abreu *et al.* 2014; Erwin *et al.* 2015). In such cases, as discussed in the accompanying observational paper (L+14), decompositions with only three components – a disc, a classical bulge and a bar – will overestimate the bulge mass to try and compensate for the omitted barlens. This effect can be very important (on average a factor of 3.5) as could be expected since the barlens can constitute a considerable part of the total mass, as shown here for simulations (see Tables 3 and 4, and Sect. 7.4) and in (L+14) for observations.

Mistaking a barlens, or part thereof, for a classical bulge can have repercussions for studies of individual galaxies. For example, in order to calculate potentials and forces within a barred galaxy in view of studying its orbital structure or the gas flow in it, we need first to obtain the volume density from the projected surface density. Here the difference between the vertical distribution of mass in barlenses and in classical bulges can make non-negligible differences in the results. Similarly, it can affect the calculation of the Q_b measure of the bar strength. Moreover, such mistakes may bias statistical studies involving galaxy classifications, and erroneously move galaxies towards earlier types. It is clear that the result of such misclassifications is a bias and not a statistical error, so that the correct fraction of disc galaxies with no classical bulge is in reality larger than so far estimated, and the contribution of classical bulges to the total baryonic mass budget considerably less. This is in good agreement with recent detailed studies which have argued that also in our Galaxy (Shen *et al.* 2010; Ness *et al.* 2013a,b), as well as in a number of nearby Sc - Scd galaxies (Kormendy *et al.* 2010) the classical bulge component is either non-existent or very small. Here we extend this statement to early type barred galaxies. A smaller contribution of classical bulges to the total baryonic mass fraction and a larger number of disc galaxies with no classical bulge

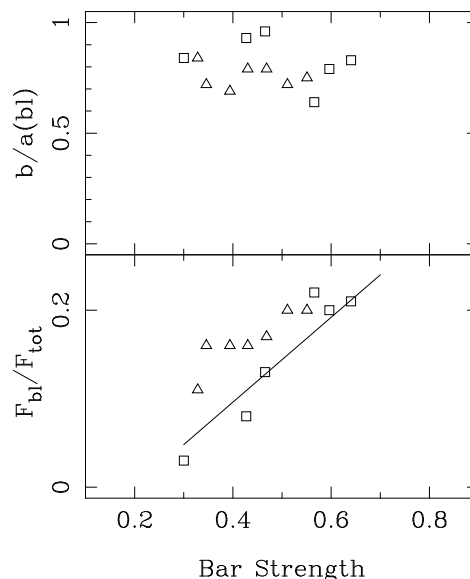


Figure 9. Evolutionary trends of barlens parameters. We display barlens axial ratio (upper panel) and barlens flux normalized by the total flux (lower panel), both as a function of bar strength. Data from gtr111 are plotted with open squares and data from gtr119 by open triangles. As the bar strength increases with time, so does the relative importance of the barlens, amounting to a bigger fraction of the total baryonic mass. The solid line is the regression line obtained from the observations (L+14). For more information see Sect. 7.4.

are facts that future galaxy formation theories will have to take into account.

7.4 Trends

In this section we will use the data we obtained in Sects. 5 and 6 to follow the temporal evolution of the barlens properties. In principle we could also check the effect of the gas fraction on the barlens, but such information is more difficult to interpret. Indeed at any given time the different simulations are at different stage of evolution, because the bar formation time depends on the gas fraction (AMR13).

In Fig. 9 we show the evolution of barlens properties as a function of time for simulations gtr111 and gtr119. In order to allow comparisons with observations we display all quantities as a function of bar strength, which is an observable quantity. How the bar strength increases with time depends strongly both on the fraction of gas in the disc component and on the halo triaxiality, being the strongest for simulations with no gas and a spherical halo, and weakest for simulations with a high gas fraction and a high halo triaxiality (AMR13). Thus, although the bar strength is not, strictly speaking, a substitute for time, it is a monotonically (though not linearly) increasing function of time⁵. The bar strength was calculated in AMR13, from the maximum of the relative $m=2$ Fourier component.

The upper panel of Fig. 9 shows the barlens axial ratio – obtained from the ellipse fits described in Sect. 5 (Table 2) – as a

⁴ Three more near-face-on galaxies with B/P/X bulges have been observed by Mendez-Abreu *et al.* (2008) and more are included in the SAURON and ATLAS3D samples.

⁵ This is true for the times in which our analysis is made, which are after peanut formation, i.e. in the secular evolution phase. At earlier times and particularly during a buckling, the bar strength is not a monotonic function of time (see Athanasoula 2013, 2015, for reviews). See also the discussion in Sect. 7.6.

function of the bar strength. No trend is visible for either gtr111 or gtr119. On the contrary, gtr101, a gas-less simulation with a spherical halo, has a very strong bar and shows a trend, with the barlens becoming more elongated with time (not shown here, but see values in Table 2). However, as we already stated, barlenses in gas-less simulations are less realistic than those in the remaining runs, and only few galaxies have such elongated barlens shapes (see also Sect. 7.1). For gtr111 and gtr119 there is no trend and the axial ratio values are in the range of 0.65 to 0.95, in good agreement with the observations (Fig. 5). Thus our simulations argue that there should be no clear evolution of the barlens shape, except perhaps for the strongest bars.

The lower panel shows the flux of the barlens component normalized by the total flux, as a function of bar strength. Simulations gtr111 and gtr119 show a clear evolution of their bar strength (AMR13) as well as of their relative barlens flux, such that there is a clear trend between these two quantities. Each simulation separately gives a much tighter fit to a straight line than the two together, because the points from the more gas-rich simulation (gtr119) are displaced above those of gtr111. Furthermore, the slopes show that the evolution of the barlens is stronger for the galaxy with less gas (gtr111). We have thus shown that the fraction of the total baryonic mass which is included in the barlens component increases noticeably with time, more so in gas-poor cases.

This global increase with time can be understood from the general growth of the bar during the secular evolution phase (Athanassoula 2013, for a review), which, as we show here, is followed by an increase of the mass of its barlens component, in good agreement with the known correlation between bar and peanut strength (Athanassoula 2008). Furthermore, the fact that the evolution for the gas poor simulation is stronger than for the gas-rich one is also in agreement with the results of AMR13, where bars in gas-poor discs were shown to evolve faster than bars in gas-rich discs.

Should we expect our predicted trends to be verified by observed galaxies? This is well possible, but not necessary. It should not be forgotten that observations may contain a much more diverse set of galaxy parameters than our models, with different masses, different disc velocity dispersions, cases with and without classical bulges, and/or a wider variety of halo mass distributions, etc, which could ‘dilute’ trends. Furthermore, simulations may cover parts of parameter space which are not relevant to real galaxies, e.g. have more extreme gas fractions or different halo shapes.

The above question – i.e. whether real galaxies verify our predicted trends – was answered in the accompanying observational paper (L+14) using a selected sub-sample of 10–15 galaxies from the NIRS0S and S⁴G samples. These show no trend for the barlens axial ratios and a very clear trend for the barlens relative flux. It is gratifying to note that these observational results confirm our predictions.

To extend the comparison further, we plotted the regression line from L+14 in the lower panel of Fig. 9. This fits very well the data from gtr111, while those of gtr119 trace a line of a somewhat smaller slope, and displaced upwards. This shows that gtr111 represents better the observations than gtr119. The main difference between the initial conditions of these two simulations is the fraction of gas in the disc component, which in the beginning of the simulation is 100% for gtr119 and 50% for gtr111. Indeed it is more realistic to assume that at the time when the disc got in place the gas fraction in it was of the order of 50% rather than 100% (e.g. Genzel et al. 2014, and references therein).

7.5 Barlens formation

We have argued that barlenses are simply the B/P/X component viewed face-on. A corollary to this would be that there are no barlenses in cases with no B/P/X. Is this indeed the case in our simulations?

To address this, we carefully examined our simulations before the B/P/X formed. Let us first note that for many simulations it is difficult to give precisely the time of B/P/X formation and that errors of at least 0.5 Gyr and often considerably larger should be expected. With that proviso let us look at a typical case in Fig. 10. Simulation gtr111 has initially 50% of its baryons in the form of gas and the evolution of its bar strength and B/P/X strength with time are given in figs 1 and 2 of Iannuzzi & Athanassoula (2015), respectively. In particular, these figures show that the peanut starts growing shortly after $t=4$ Gyr, with a best estimate of $t=4.5$ Gyr. Thus the right-hand panel of Fig. 10, at $t=6$ Gyr is well after the time when the B/P/X started growing, as is asserted also by the corresponding upper subpanel, where the peanut structure is clear. At this time the face-on view (lower subpanel of the right-hand column) clearly displays a barlens component. At $t=3.5$ Gyr (left-hand column), i.e. before the B/P/X started growing, this simulation shows no barlens component, while at $t=4$ (middle panel) – i.e. roughly at the moment where the B/P/X starts growing, or slightly before it – we see that the barlens starts becoming visible.

This and other examples from our simulations argue that, at least for the models that we have analysed here, the barlens and the B/P/X grow roughly concurrently, but shifts of the order of half or one Gyr can not be excluded. Early on, at times when the B/P/X has clearly not started growing, no barlens is visible in the simulations. This means that some of the observed bars, the relatively youngest ones, will not have a barlens component, in good agreement with the observation result of Laurikainen *et al.* (2013), who found that not all barred galaxies have barlenses. Furthermore, it argues that all galaxies with a barlens component must be in their secular evolution phase.

7.6 The orbital structure of barlenses

The first step to understanding the dynamics of any substructure is to study the orbits that constitute it. No specific study of orbits in barlenses has so far been made, but since these structures are the face-on view of the B/P/X bulges, as we argued in this paper, the orbital structure of the latter (discussed e.g. by Pfenniger 1984; Patsis *et al.* 2002, Skokos *et al.* 2002a and Patsis & Katsanikas 2014; see also Athanassoula 2015 for a review) should provide the necessary information. The most likely building blocks for our case and the most widely discussed in the literature, will then be 3D families of periodic orbits of the x_1 tree which bifurcate from the vertical resonances of the 2D x_1 family and have stable parts of a sufficiently large extent. The families that bifurcate at the lowest energies – such as x_1v_1 , x_1v_3 , x_1v_4 , or x_1v_5 – are the most likely candidates, since the outline of orbits from higher order bifurcating families are less vertically extended and more extended along the bar major axis, and thus less appropriate building blocks. An alternative would be the $z3.1s$ family (Skokos *et al.* 2002b), whose orbits have a morphology similar to that of the x_1v_4 family but is not related to the x_1 tree. This, however, would be suitable only in specific models, while B/P/X bulges are more generally found in barred models. This alternative is therefore not very likely and we will not consider it further here.

As mentioned above, orbits from families bifurcating from the

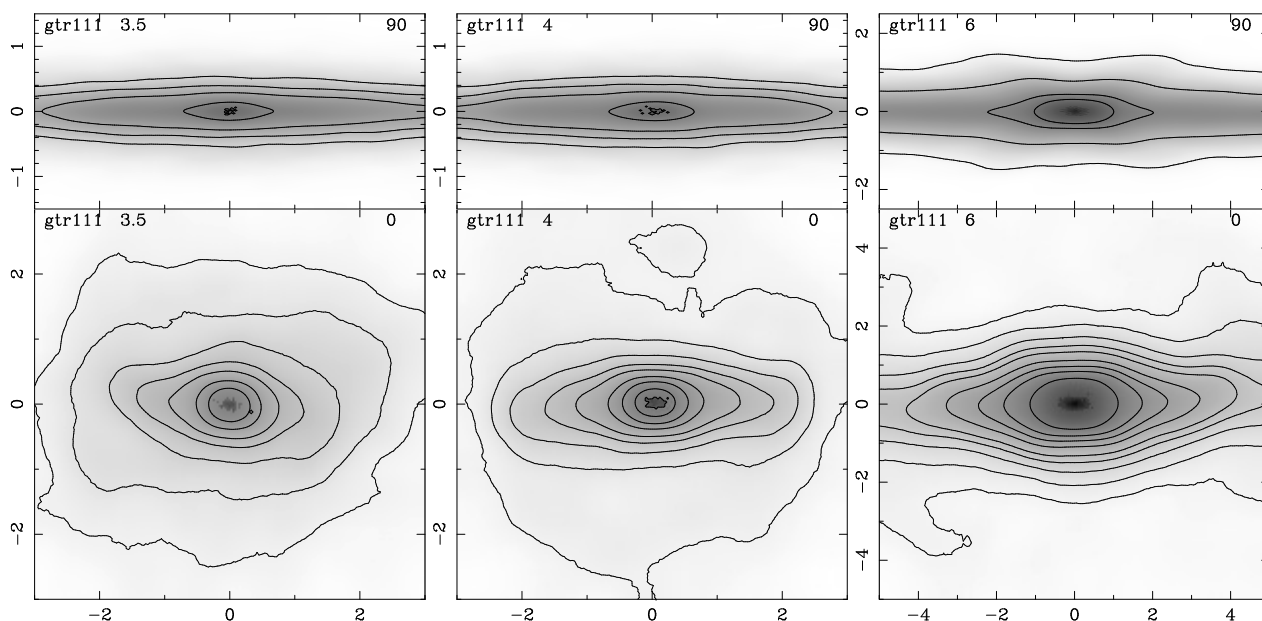


Figure 10. Grey-scale plots and isodensities of face-on (lower panels) and edge-on (upper panels) views of simulation gtr111. From left to right the corresponding times are 3.5, 4 and 6 Gyr. The grey-scale levels are logarithmically spaced and the isodensities are at levels chosen to show best given morphological features discussed in the text. In the upper left corner of each sub-panel we give the simulation name and snapshot time and in the upper right one the viewing inclination angle in degrees. Note that in the rightmost panel the linear scale is different from that of the other two panels, so as to follow the growth of the bar.

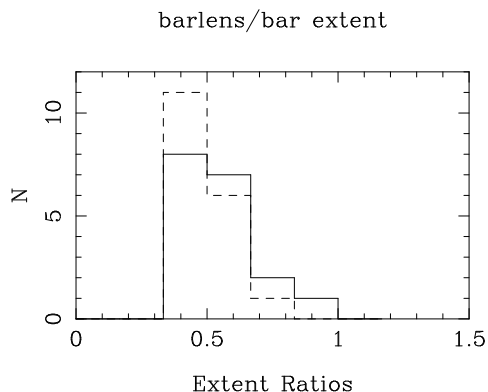


Figure 11. Histogram of the ratio of the extent of the barlens to that of the thin part of the bar. The solid line gives the histogram for the extent ratios given in Table 1, i.e. using the same method as previously used for the NIRS0S observations, while the dashed line gives the histogram of the same quantity, but with measurements obtained from the face-on and side-on isodensity curves, as described in Sect. 7.2.

x_1 at low energies (low values of the Jacobi constant) are less extended along the bar major axis compared to the thin part of the bar than orbits from higher order families. Thus, by comparing the horizontal extent of the barlens to that of the thin bar component, we should in principle be able to deduce which vertical resonance is the main contributor to the barlens and where it is located. In practice, however, this is not easy because the relative extent of the orbits of various families is model dependent. In Table 1 we gave values for the ratio of the barlens extent to that of the thin bar component for the $t=6$ Gyr snapshots of all simulations discussed here and in Fig. 11 we give a histogram of these values (solid line). As already mentioned in Sect. 7.1, all but one of the snapshots have extent ratios within the range defined by the NIRS0S observations. The

exception is gcs006, whose measurement, as discussed in Sect. 5.2, is not as reliable as the rest.

Our next step will be to compare the values of the extent ratios with the corresponding numbers found from orbital structure work. In particular we want to compare them with the corresponding numbers in tables 1 to 6 of Patsis *et al.* (2002). These set rough limits to the extent ratios depending on the main family that constitutes the barlens. For example for x_1v_1 the ratio of barlens to bar extent should be less than 0.5, while for the other families it should be larger than 0.6 and less than 1. As we will discuss below, there is always some uncertainty in these numbers, because the orbits were calculated in a fiducial potential and not in the potential of each given galaxy and, furthermore, the measurements of the barlens and bar extent always have some measuring error.

Fig. 11 shows that, making a conservative estimate of a 10% global uncertainty, only 3 out of 18 models have $L(\text{bl}) / L(\text{bar})$ which is not compatible with the x_1v_1 family. The three exceptions are gtr101, gtr117 and gcs006, which have extent ratios of 0.77, 0.81 and 0.94, respectively. Note that the measurements given for these three cases are less reliable than the remaining ones, as discussed in Sect. 5.2 and 6.3.2. Thus, our results indicate that in about 83% of our simulations, and perhaps more, the x_1v_1 family can be the backbone of the B/P/X/bl component. This number is not in good agreement with the NIRS0S results, where this fraction is lowered to about 54%. The disagreement is not surprising. As already mentioned, our simulations covered the gas fraction and halo shape parameter space homogeneously, so as to better explain their effect on bar formation and evolution. They did not attempt to model specific galaxies, nor did they attempt to follow their distributions in parameter space. Thus the distribution of any result, such as the extent ratios, can not be expected to be similar in observations and in simulations. There is, nevertheless, good agreement between the two because the ranges of values covered by observations and simulations are in good agreement, as we already showed in Sect. 7.1.

In Sect. 7.2 we used the isodensity curves in the side-on view to measure the B/P extent, and found that the results agreed very well with those obtained for the barlens from the face-on view given in Sect. 5. Similarly, the extent of the bar can be measured from the isodensity curves in the face-on view. We compared the latter results with the bar length measurements obtained with the method used in the NIRSOS analysis (see Sect. 5) and found differences. These differences are not due to different personal appreciation, but are systematic, due to differences between methods. Indeed the isodensity method places the end of the bar further out than the ridge line of the ring. The median value of the ratio of the bar length as obtained with the NIRSOS rule to that obtained from the isodensity shapes is 0.86, and the mean 0.87, with an absolute deviation of 0.11. We then calculated the ratios of barlens extent to bar length using for both quantities the values obtained by the isodensities and plot the result in Fig. 11 (dashed line). As expected, the values of the extent ratios are smaller, so the histogram is somewhat shifted. Now only two simulations have a ratio beyond 0.6, namely gtr101 and gcs006, with ratios 0.62 and 0.73, respectively. These two simulations have no gas and their measurements are less accurate than those of the rest. We may thus conclude that a very large fraction, if not all the simulations could have a B/P/X/bl feature compatible with the $x_1 v_1$ family.

Some care, however, has to be taken when using results from orbital structure theory to make detailed quantitative comparisons with observations. Bars have a very complex morphology and geometry and, as a result, their potential has not been yet adequately modelled analytically. The most realistic of the existing analytic models, the Ferrers models (Ferrers 1877), have an ellipsoidal face-on shape, which is not a good description of the real bar shape (Athanassoula *et al.* 1990; Gadotti 2009, 2011), and, viewed edge-on, do not have a B/P/X. Yet, for lack of any better potential/density model, Ferrers models have been used in most orbital structure studies of the barlens/bar/bulge region (e.g. Athanassoula *et al.* 1983; Papayannopoulos & Petrou 1983; Pfenniger 1984; Athanassoula 1992; Skokos *et al.* 2002a,b; Patsis 2005). The main qualitative results of these studies should be applicable to real galaxies, but at least some of their quantitative results may not be sufficiently accurate for detailed comparisons with observations. It would therefore be highly desirable to find analytic galactic potentials that take into account both the 3D shape of the B/P/X/barlens component and the rectangularity of the thin bar component, in order to make yet more realistic orbital structure studies.

Skokos *et al.* (2002a) noted that the (x, y) projections of the 3D families of the x_1 -tree, i.e. the $x_1 v_n$, $n = 1, 2, 3, \dots$ families, retain a morphological similarity with the parent x_1 family at the same energy, in particular in regions relatively near the bifurcating points. This could, at first sight, have been considered to disagree with the fact that the face-on outlines of the barlens are very different from that of the thin bar components, and thus argue against the barlens picture that we propose here. It must, however, be kept in mind that the orbital structure study of Skokos *et al.* (2002a), like those of all other such studies, is carried out using Ferrers potentials and does not include the potential of a separate barlens components. This is a further argument underlining the necessity of orbital structure studies using yet more realistic potentials.

7.7 Discy bulges

We have so far discussed at length the links between B/P/X bulges and barlenses and also mentioned tentatively that, if no appropriate kinematic or photometric data are available, barlenses could be

confused with classical bulges. There is, however, yet another type of bulges which we have not discussed yet, namely discy pseudo-bulges (Kormendy & Kennicutt 2004; Athanassoula 2005; Erwin 2008). These have the shape of a thin disc and a large fraction of their mass is in gas and relatively young stars. Could they, like the classical bulges, be mistaken for a barlens? We think this is unlikely, for many reasons, of which the most important is that their sizes are much smaller than that of the barlenses, only of the order of 1 kpc or even smaller (e.g. Kormendy & Kennicutt 2004; Athanassoula 2005). Furthermore, their populations are on average younger than that of barlenses.

Given their possible formation scenarios, it is expected that the various types of bulges will very often co-exist (Athanassoula 2005) and this was indeed shown to be true by observations (Kormendy & Barentine 2010; Nowak *et al.* 2010; Mendez-Abreu *et al.* 2014; Erwin *et al.* 2015). Could co-existing classical and discy bulges in galaxies with a bar but no B/P/X bulge give structures having the properties of barlenses? We have at our disposal no simulations with the adequate structures – i.e. no appropriate simulations with both classical and discy bulges – to examine this question in depth. However, in view of the arguments we gave above on the inadequacy of discy bulges to provide reasonable building blocks for barlenses, this does not seem likely.

Of course discy bulges and barlenses can co-exist (see references in the previous paragraph). In such cases a number of structures of limited radial extent, such as nuclear spirals, nuclear rings and nuclear bars, will be seen in the central parts of the barlenses, but will in fact be part of the discy bulge (e.g. Laurikainen *et al.* 2013, L+14), not of the barlens itself.

8 SUMMARY

In this paper we used snapshots of barred disc galaxy simulations to make images, which we then analysed using the same procedures and software as for the analysis of real galaxy images in previous studies. We found that our simulations can produce components with properties comparable to those of observed barlenses. By making a number of comparisons between simulations and observations – including morphology, radial projected density profiles, shapes obtained from ellipse fits and decomposition results – we find very good agreement and thus reach the conclusion that our simulations are sufficiently realistic to describe accurately components such as barlenses.

Viewing our simulations both face-on and edge-on we were able to explore the nature of the barlens component and to find that *the barlens and the B/P/X bulge are one and the same component, but viewed from a different angle*. We found this to be true not only for elongated barlenses, but also for the case of near-circular ones.

This result concerning the nature of the barlens component implies that the distribution of the z -component of the velocity of stars in the barlens should correspond to that of a vertically thick object, while that of the stars in the thin component should be that of a vertically thin one. It should be possible to test this prediction by measuring the vertical velocity component along the bar major axis of appropriately chosen face-on barred galaxies. One should then find a much higher velocity dispersion σ_z and a different structure of the higher velocity moments in the thick barlens component compared to the thin part of the bar (Iannuzzi & Athanassoula 2015). It is not, however, necessary to expect that there should be a sharp transition between the two regions. Indeed, in Sect. 4 we found that there is no such sharp transition in the radial luminosity profile along the

bar major axis, and we attributed this to the fact that the thin bar component continues inwards into the barlens region. Thus, in the region surrounding the bar major axis and within the barlens component there will be contributions from both components, leading to a smooth transition.

Our result has a further implication, namely that it can set a rough lower limit of the bar age and a very clear one on the phase of evolution the bar is in. Indeed, the fact that the barlens and the boxy/peanut bulge are one and the same component implies that for the barlens to exist, the B/P/X must have already formed. Therefore, the bar must be in the secular evolution phase, i.e. between one and a few Gyr must have elapsed from the moment it started forming, as was discussed in Sect. 7.5.

For all the simulations discussed here, the most realistic barlenses were found when there is between 20 and 80 per cent gas in the initial conditions. Collisionless simulations, i.e. simulations whose initial conditions contain no gas, have barlenses which are too extended compared to observations and it is not even clear whether using a second bar component in the decomposition improves the fit. This could be expected because real galaxies will normally contain some gas when the bar grows, except for the rather unlikely case when all the gas is consumed before the bar starts growing and there is no accretion to add more (AMR13, Athanassoula 2014). At the other extreme, simulations with initially 100% gas have very short thin bar components, so that they are more reminiscent of barlenses in non-barred galaxies. Note also that, for such high initial gas fractions, the trend between the fraction of the total flux which is in the barlens component and the bar strength has a smaller slope than the observations and is considerably offset towards larger barlens fluxes.

The morphology of the barlens component is such that in some cases it can be mistaken for a classical bulge, unless high resolution and high quality photometry and/or kinematics are available. Furthermore, not including a barlens in decompositions can artificially increase the bulge-to-total ratio by, on average, a factor of 3.5 (L+14). This is due to the classical bulge compensating for the lack of the barlens component. Thus the number of galaxies with no classical bulge is higher than what has been so far assumed and also in many galaxies the contribution of the classical bulge to the total mass budget is substantially lower than what has been so far estimated. This can introduce errors in dynamical studies of some individual galaxies and a bias in a number of statistical studies. We propose that photometry and particularly kinematics can be used to distinguish between classical bulges and barlenses and thus avoid misclassifications.

We also give a rule of thumb to obtain the extent of the barlens component in the direction of the bar major axis, for relatively low inclination galaxies. This, however, will not work for all possible morphologies, as for example cases where the isodensities of the bar are concentric thick ellipses. We showed that in most of the simulations considered in this paper, the B/P/X/bl component is compatible with a x_1v_1 backbone, provided the Ferrers models can be considered sufficiently realistic. On the other hand, the fraction of real galaxies compatible with an x_1v_1 barlens backbone could be considerably smaller, of the order of 50–60%.

We also found a trend between the fraction of the total flux that is in the barlens component and the strength of the bar, which argues that during the secular evolution phase, as the bar grows stronger the barlens component also becomes more important, so that it represents an increasing fraction of the baryonic mass. This trend is confirmed by observations. The quantitative comparison is best for a model with 50%, rather than 100% initial gas fraction,

which is indeed in better agreement with observations (e.g. Genzel et al. 2014, and references therein).

All our tests confirm that barlenses can be considered as face-on B/P/X bulges. We do not, however, claim that this is the only possible alternative, i.e. that there is no other way to explain barlenses. Indeed, proving uniqueness is very difficult, if not impossible for the formation of galaxies, or of their components and we can not exclude that another alternative will be brought up in the future. We did, nevertheless, outline some of the serious problems that alternatives based on a discy bulge component would face.

Our work also underlines the necessity of a further improvement. Namely, a considerable part of orbital structure studies and of gas flow calculations should be revisited using yet more realistic potentials, which take into account the complex 3D structure of bars and include the vertical structure of the B/P/X/bl component.

ACKNOWLEDGEMENTS

We thank the referee for his/her comments, Volker Springel for making available to us the version of GADGET used here and Jean-Charles Lambert for the GLNEMO software (<http://projets.oamp.fr/projects/glnemo2>). All authors acknowledge financial support to the DAGAL network from the People Programme (Marie Curie Actions) of the European Union's Seventh Framework Programme FP7/2007-2013/ under REA grant agreement number PITN-GA-2011-289313. EA and AB also acknowledge financial support from the CNES (Centre National d'Etudes Spatiales - France) and from the 'Programme National de Cosmologie and Galaxies' (PNCG) of CNRS/INSU, France. EA acknowledges the use of HPC resources from GENCI- TGCC/CINES (Grants 2013 - x2013047098 and 2014 - x2014047098). EL and HS acknowledge support from the Academy of Finland. This research is based in part on observations made with the Spitzer Space Telescope, which is operated by the Jet Propulsion Laboratory, California Institute of Technology under a contract with NASA.

Funding for the SDSS and SDSS-II has been provided by the Alfred P. Sloan Foundation, the Participating Institutions, the National Science Foundation, the U.S. Department of Energy, the National Aeronautics and Space Administration, the Japanese Monbukagakusho, the Max Planck Society, and the Higher Education Funding Council for England. The SDSS Web Site is <http://www.sdss.org/>. The SDSS is managed by the Astrophysical Research Consortium for the Participating Institutions. The Participating Institutions are the American Museum of Natural History, Astrophysical Institute Potsdam, University of Basel, University of Cambridge, Case Western Reserve University, University of Chicago, Drexel University, Fermilab, the Institute for Advanced Study, the Japan Participation Group, Johns Hopkins University, the Joint Institute for Nuclear Astrophysics, the Kavli Institute for Particle Astrophysics and Cosmology, the Korean Scientist Group, the Chinese Academy of Sciences (LAMOST), Los Alamos National Laboratory, the Max-Planck-Institute for Astronomy (MPIA), the Max-Planck-Institute for Astrophysics (MPA), New Mexico State University, Ohio State University, University of Pittsburgh, University of Portsmouth, Princeton University, the United States Naval Observatory, and the University of Washington.

REFERENCES

- Aguerri, J. A. L., Balcells, M., Peletier, R. F. 2001, *A&A*, 367, 428
- Athanassoula, E., 1992, *MNRAS*, 259, 328
- Athanassoula E., 2003, *MNRAS*, 341, 1179
- Athanassoula, E., 2005, *MNRAS*, 358, 1477
- Athanassoula, E., 2006, arXiv:astro-ph/0610113
- Athanassoula, E., 2008, in “Formation and Evolution of Galaxy Bulges”, *Proc. IAU Symposium*, 245, 93
- Athanassoula, E., 2013, in “Secular Evolution of Galaxies”, J. Falcón-Barroso and J. Knapen (eds.), Cambridge University Press, Cambridge, 305.
- Athanassoula, E., 2014, *MNRAS*, 438, 81
- Athanassoula, E., 2015, in “Galactic Bulges”, E. Laurikainen, R. Peletier and D. Gadotti (eds.), Springer Verlag, Chapter 14
- Athanassoula, E., Beaton, R. L. 2006, *MNRAS*, 370, 1499
- Athanassoula, E., Bienaymé, O., Martinet, L. & Pfenniger, D. 1983, *A&A*, 127, 349
- Athanassoula, E., Machado, R. E. G., & Rodionov, S. A. 2013, *MNRAS*, 429, 1949 (AMR13)
- Athanassoula, E., Misiriotis A., 2002, *MNRAS*, 330, 35
- Athanassoula, E., Morin, S., Wozniak, H., Puy, D., Pierce, M. J., Lombard, J., Bosma, A. 1990, *MNRAS*, 245, 130
- Beaton, R. L., Majewski, S. R., Guhathakurta, P., Skrutskie, M. F., Cutri, R. M., Good, J., Patterson, R. J., Athanassoula, E., Bureau, M. 2007, *ApJ*, 658, L91
- Benjamin, R. J. et al., *ApJ*, 630, L149
- Berentzen I., Heller C. H., Shlosman I., Fricke K. J., 1998, *MNRAS*, 300, 49
- Berentzen I., Shlosman I., Martinez-Valpuesta I., Heller C. H., 2007, *ApJ*, 666, 189
- Bettoni, D., Galletta, G., 1994, *A&A*, 281, 1
- Binney, J. 1978, *MNRAS*, 183, 501
- Bureau, M., Aronica, G., Athanassoula, E., Dettmar, R.-J., Bosma, A., Freeman, K. C. 2006, *MNRAS*, 370, 753
- Buta, R. 2013a, *Planets, Stars and Stellar Systems Vol. 6*, Eds. Oswalt, Terry D.; Keel, William C., Springer, Dordrecht, p. 1
- Buta, R. 2013b, in *Falcon-Barroso J., Knapen J., eds., Secular Evolution of Galaxies*, Cambridge Univ. Press, Cambridge, p. 155
- Buta, R., Laurikainen E., Salo H., Block, D. L., Knapen J. H., 2006, *AJ*, 132, 1859
- Cabrera-Lavers, A., González-Fernández, C., Garzón, F., Hammersley, P.L., López-Corredoira, M. 2008, *A&A*, 491, 781
- Cabrera-Lavers, A., Hammersley, P. L., González-Fernández, C., López-Corredoira, M., Garzón, F., Mahoney, T. J. 2007, *A&A*, 465, 825
- Cappellari, M. et al. 2011, *MNRAS*, 416, 1680
- Cappellari, M. et al. 2013, *MNRAS*, 432, 1862
- Churchwell, E., Babler, B.L., Meade, M.R., Whitney, B.A., Benjamin, R., Indebetouw, R., Cyganowski, C., Robitaille, T.P., Povich, M., Watson, C., Bracker, S. 2009, *PASP*, 121, 213
- Coelho, P., Gadotti, D. A. 2011, *ApJ*, 743, 13
- Combes, F., Debbasch, F., Friedli, D., Pfenniger D., 1990, *A&A*, 233, 82
- Combes F., Sanders R. H., 1981, *A&A*, 96, 164
- Contopoulos, G., Papayannopoulos, T. 1980, *A&A*, 92, 33
- Debattista V. P., Carollo C. M., Mayer L., Moore B., 2004, *ApJ*, 604, L93
- Drory, N., Fisher, D. B. 2007, *ApJ*, 664, 640
- Elmegreen B. G., Elmegreen D. M., 1985, 1985, *ApJ*, 288, 438
- Erwin, P., 2008, in *Formation and Evolution of Galaxy Bulges*, *Proc. IAU Symp.* 245, eds. M. Bureau, E. Athanassoula & B. Barbuy, Cambridge University Press, Cambridge, 113
- Erwin, P., Sparke, L. 2003, *ApJS*, 146, 299
- Erwin, P., Debattista, V. 2013, *MNRAS*, 431, 3060
- Erwin, P. et al. 2015, *MNRAS*, 446, 4039
- Ferrers N. M. 1877, *Q.J. Pure Appl. Math.*, 14, 1
- Fisher, D. B., Drory, N. 2008, *ApJ*, 136, 773
- Gadotti D. A., 2008, *MNRAS*, 384, 420
- Gadotti, D. A., 2009, in ‘Chaos in Astronomy’, G. Contopoulos and P. Patsis (eds), Springer Berlin, 159
- Gadotti D. A., 2011, *MNRAS*, 415, 3308
- Genzel, R. A. et al. 2015, *ApJ*, 800, 20
- Hammersley, P. L., Garzón, F., Mahoney, T. J., López-Corredoira, M., M.A.P. Torres, M. A. P. 2000, *MNRAS*, 317, L45
- Hernquist L., 1993, *ApJS*, 86, 389
- Iannuzzi F., Athanassoula, E. 2015, *MNRAS*, 450, 2514
- Kim, T. et al. 2015, *ApJ*, 799, 99
- Kent, S., Glaudel, J. 1989, *AJ*, 98, 1588
- Kormendy J. 1979, *ApJ*, 227, 714
- Kormendy J. 1983, *ApJ*, 275, 529
- Kormendy J. 1984, *ApJ*, 286, 183
- Kormendy J., Drory N., Bender R., Cornell M. 2010, *ApJ*, 723, 54
- Kormendy J., Kennicutt R. C., Jr., 2004, *ARA&A*, 42, 603
- Kormendy, J., Barentine, J. 2010, *ApJ*, 715, 176
- Laurikainen, E., Salo, H. 2015, in “Galactic Bulges”, E. Laurikainen, R. Peletier and D. Gadotti (eds.), Springer Verlag, Berlin, Chapter 4
- Laurikainen, E., Salo, H., Athanassoula, E., Bosma, A., Herrera Endoqui, M. 2014, *MNRAS*, 444, 80 (L+14)
- Laurikainen, E., Salo, H., Athanassoula, E., Bosma, A., Buta, R., Janz, J. 2013, *MNRAS*, 430, 3489
- Laurikainen, E., Salo, H., Buta, R. 2005, *MNRAS*, 362, 1319
- Laurikainen, E., Salo, H., Buta, R., Knapen, J., Speltinckx, T.; Block, D. 2005, *AJ*, 132, 2634
- Laurikainen, E., Salo, H., Buta, R., Knapen, J. 2007, *ApJ*, 692, 34
- Laurikainen, E., Salo, H., Buta, R., Knapen, J. 2009, *MNRAS*, 381, 401
- Laurikainen, E., Salo, H., Buta, R., Knapen, J. 2011, *MNRAS*, 418, 1452
- Laurikainen, E., Salo, H., Buta, R., Knapen, J., Comerón, S. 2010, *MNRAS*, 405, 1089
- López-Corredoira, M., Cabrera-Lavers, A., Mahoney, T.J., Hammersley, P.L., Garzón, F., González-Fernández, C. 2007, *AJ*, 133, 154
- Lütticke, R., Dettmar, R.-J., Pohlen, M., 2000, *A&A*, 362, 435
- Martinez-Valpuesta I., Shlosman I., Heller C., 2006, *ApJ*, 637, 214
- Meidt, S. et al. 2012a, *ApJ*, 744, 17
- Meidt, S. et al. 2012b, *ApJ*, 748, 30L
- Meidt, S. et al. 2014, *ApJ*, 788, 144
- Méndez-Abreu, J., Corsini, E. M., Debattista, Victor P., De Rijcke, S., Aguerri, J. A. L., Pizzella, A. 2008, *ApJ*, 679, 73
- Mendez-Abreu, J., Debattista, V. P., Corsini, E. M., Aguerri, J. A. L. 2014, *A&A*, 572, 25
- Martínez-Valpuesta, I., Gerhard, O. 2011, *ApJL*, 734, L20
- Martínez-Valpuesta, I., Knapen, J., Buta, R. 2007, *AJ*, 134, 1863
- Navarro J.F., Frenk C.S., White S.D.M., 1996, *ApJ*, 462, 563
- Navarro J.F., Frenk C.S., White S.D.M., 1997, *ApJ*, 490, 493
- Ness et al. 2013a, *MNRAS*, 430, 836
- Ness et al. 2013b, *MNRAS*, 432, 2092

- Nowak, N., Thomas, J., Erwin, P., Saglia, R. P., Bender, R., Davies, R. I. 2010, MNRAS, 403, 646
- Papayannopoulos, T., Petrou, M. 1983, A&A, 119, 21
- Patsis, P. A., 2005, MNRAS, 358, 305
- Patsis P. A., Katsanikas M., 2014, MNRAS, 445, 3546
- Patsis, P. A., Skokos, Ch., Athanassoula, E. 2002, MNRAS, 337, 578
- Peng, C. V., Ho, L. C., Impey, C. D., Rix, H.-W. 2010, AJ, 139, 2097
- Pfenniger, D. 1984, A&A, 134, 373
- Pfenniger, D., Friedli, D. 1991, A&A, 252, 75
- Querejeta, M. 2015, ApJS, 219, 5
- Quillen, A. C., Kuchinski, L. E., Frogel, J. A., DePoy, D. L., 1997, ApJ, 481, 179
- Raha N., Sellwood J. A., James R. A., Kahn F. D., 1991, Nature, 352, 411
- Rodionov S. A., Athanassoula E., 2011, A&A, 529, A98
- Rodionov S. A., Athanassoula E., Sotnikova N. Y., 2009, MNRAS, 392, 904
- Romero-Gómez, M., Athanassoula, E., Antoja, T., Figueras, F. 2011, MNRAS, 418, 1176
- Salo, H. et al. 2015, ApJS, 219, 4
- Sandage, A. 1961, The Hubble Atlas of Galaxies, Carnegie Institution, Washington
- Shen, J., Rich, M., Kormendy, J., Howard, C., De Propris, R.; Kunder, A. 2010, ApJ, 720, 72
- Sheth, K. et al. 2010, PASP, 122, 1397
- Skokos, Ch., Patsis, P. A., Athanassoula, E. 2002a, MNRAS, 333, 847
- Skokos, Ch., Patsis, P. A., Athanassoula, E. 2002b, MNRAS, 333, 861
- Springel V., 2005, MNRAS, 364, 1105
- Springel V., Hernquist L., 2002, MNRAS, 333, 649
- Springel V., Hernquist L., 2003, MNRAS, 339, 289
- Springel V., Yoshida N., White S. D. M., 2001, New Astron., 6, 79
- Wakamatsu, K. I., Hamabe, M. 1984, ApJS, 56, 283